



Oil behavior in sea ice: Changes in chemical composition and resultant effect on sea ice dielectrics



Durell S. Desmond*, Diana Saltymakova, Thomas D. Neusitzer, Nariman Firoozy, Dustin Isleifson, David G. Barber, Gary A. Stern*

University of Manitoba, Winnipeg, MB, Canada

ARTICLE INFO

Keywords:
Arctic sea ice
Petroleum hydrocarbons
Oil composition
Oil weathering
Dielectrics
Remote sensing

ABSTRACT

There has been increasing urgency to develop methods for detecting oil in sea ice owing to the effects of climate change in the Arctic. A multidisciplinary study of crude oil behavior in a sea ice environment was conducted at the University of Manitoba during the winter of 2016. In the experiment, medium-light crude oil was injected underneath young sea ice in a mesocosm. The physical and thermodynamic properties of the oil-infiltrated sea ice were monitored over a three-week time span, with concomitant analysis of the oil composition using analytical instrumentation. A resonant perturbation technique was used to measure the oil dielectric properties, and the contaminated sea ice dielectric properties were modeled using a mixture model approach. Results showed that the interactions between the oil and sea ice altered their physical and thermodynamic properties. These changes led to an overall decrease in sea ice dielectrics, potentially detectable by remote sensing systems.

1. Introduction

Within the Arctic, a persistent decrease in sea-ice extent and transition to annual ice types (MacDonald, 1988; Lashof, 1989; Jones and Henderson-Sellers, 1990; Walsh et al., 2005; Kwok et al., 2009; Maslanik et al., 2011; Galley et al., 2016) has resulted in shipping routes and oil exploration in the Arctic becoming increasingly more feasible. The increase in shipping traffic raises the risk of crude oil or fuel being spilled into the marine environment (AMAP, 2010; Harsem et al., 2011; Schenk, 2011; Smith and Stephenson, 2013). This rising risk poses a threat to marine ecosystems and local inhabitants due to the oil's toxic nature and persistence (Wiese et al., 2004; Fritt-Rasmussen et al., 2015; Anderson et al., 1974). Hence, there exists an urgency to develop methods for detecting and monitoring potential oil spills in Arctic waters, thus allowing for fast response times to mitigate and minimize the extent of damage.

Remote sensing systems have been used to assist in locating and tracking oil for forensic purposes for over 47 years (Swaby and Forziati, 1969). However, sensors for detecting oil in or under ice and snow are currently inadequate, and only a few novel remote sensing technologies show potential for oil spill detection in the ice-covered sea (Brown and Fingas, 2003; Brekke et al., 2014; Wilkinson et al., 2015; Bradford et al., 2015; Firoozy et al., 2017). Sea ice is a heterogeneous porous media consisting of an ice matrix in which is embedded liquid brine inclusions

and air bubbles. The presence of a brine network and air inclusions greatly complicate the interactions and movements governing oil within the sea ice cover (Fingas and Brown, 2007). Furthermore, weathered oil can have significantly different chemical properties relative to its parent mixture. Major short-term weathering processes such as evaporation, dispersion, and emulsification govern the overall physical behavior of the surface slick (e.g., viscosity and volume density) and the mass balance of the oil spill. Longer term processes such as dissolution, biodegradation, and photo-oxidation will alter the structure and molecular weight (MW) of individual compounds which, in turn, will affect their vapor pressures and water solubilities (Simecek-Beatty and Lehr, 2007; Wang and Stout, 2007). In an Arctic setting, the rates of evaporation and dissolution will be significantly different relative to a warmer climate; as the air and water temperatures are lower in the Arctic, evaporation rates will be slower and potentially negligible if the oil is either underneath or encapsulated within the ice (Fingas and Hollebone, 2003; Brandvik and Faksness, 2009; Brandvik et al., 2006). Furthermore, dissolution processes may become more important, due to the impedance of evaporation, as more of the volatile components which are also water soluble may have an increased tendency to partition into the water column (Faksness et al., 2008; Faksness and Brandvik, 2008; Payne et al., 1991a; Payne et al., 1991b). These processes are essential in the understanding of how oil chemistry and physics, as it pertains to the interaction of oil and ice over time, may

* Corresponding authors.

E-mail addresses: umdesmod@umanitoba.ca (D.S. Desmond), Gary.stern@umanitoba.ca (G.A. Stern).

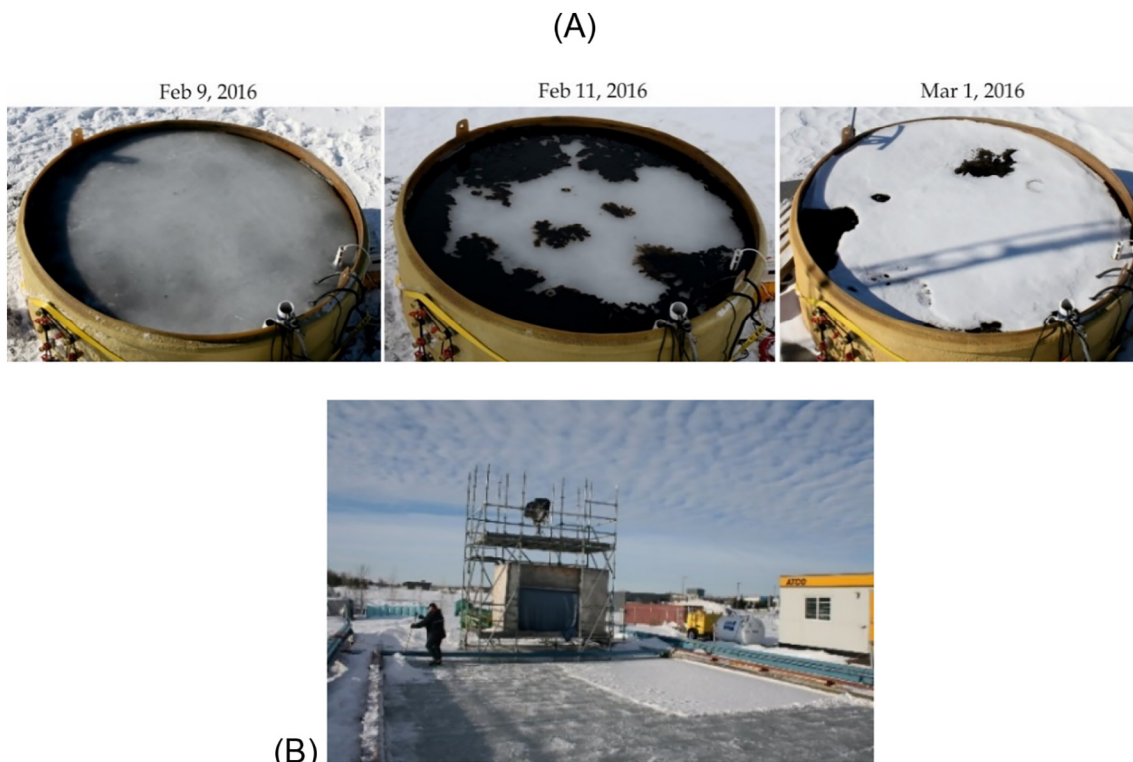


Fig. 1. (A) Insulated fiberglass tank used to facilitate the artificial oil-in-ice mesocosm depicting the oil evolution and alteration of the ice surface during the second phase of the experiment (Neusitzer et al., 2018). (B) The main SERF pool positioned directly in front of the C-band polarimetric scatterometer platform which is situated directly in front of the oil pool.

alter or impact representative electromagnetic radiation and acoustic signatures of remote sensing technologies.

Over the years, there has been a moderate number of studies conducted on the interactions, behaviors, and effects of crude oil in sea ice (e.g. Fingas and Hollebone, 2003; Faksness et al., 2008; Brandvik et al., 2009; Faksness et al., 2011; Nemirovskaya, 2014; Scheibye et al., 2017; Ballesteros and Magdol, 2011; Faksness and Brandvik, 2008; Mauz et al., 2015; Petrich et al., 2013; Afenyo et al., 2016a; Afenyo et al., 2016b; Brandvik et al., 2006; Nordam et al., 2018; Payne et al., 1991a; Payne et al., 1991b; Petrich et al., 2018; Sadnick et al., 2017; Vergeynst et al., 2019; Word et al., 2011; Boccadoro et al., 2018). Much of the research that has been accomplished has focused on bulk physical movement tendencies and changes made to the physical properties of different oil types due to weathering (macroscopic behavior) (e.g., Afenyo et al., 2016a; Afenyo et al., 2016b; Brandvik et al., 2006). Less research has, however, focused on microscopic behavior, including transformations and distributions for an extensive list of monitored compounds within and from the sea ice (e.g., Payne et al., 1991a; Payne et al., 1991b; Vergeynst et al., 2019; Desmond, 2018; Faksness and Brandvik, 2008; Ballesteros and Magdol, 2011; Boccadoro et al., 2018). Notably, far fewer studies have investigated the effect of oil on sea ice temperature and salinity (e.g., Payne et al., 1991b; Sadnick et al., 2017; Desmond, 2018) and more importantly on sea ice dielectrics (complex permittivity) (Brown and Fingas, 2003; Brekke et al., 2014; Firoozy et al., 2017; Firoozy et al., 2018; Neusitzer et al., 2018; Desmond, 2018); an important parameter associated with various remote sensing technologies such as active radar, which utilizes the normalized radar cross section of sea ice (dependent on sea ice dielectrics), for oil spill detection (Brown and Fingas, 2003; Firoozy et al., 2017; Firoozy et al., 2018; Neusitzer et al., 2018). More research is therefore required to fully grasp the physical and chemical processes and impacts of oil in a sea ice environment both on a macroscopic as well as a microscopic scale. The Arctic ice pack is known to be a complex environment integrating several components (e.g., snow, first-year ice, multi-year ice,

and seawater), each with their respective dielectric constants (1 to 2, 3 to ~ 5 , ~ 3 , and ~ 80 respectively) (Fingas and Brown, 2007). In light of this, it is speculated that inclusion of crude oil (dielectric constant of 2 to 3) (Fingas and Brown, 2007) will lower the overall sea ice dielectrics directly through its initial presence and indirectly through a subsequent change of sea ice temperature and salinity, both of which are essential parameters of dielectrics. It is further postulated that the weathering effects of dissolution and compound partitioning within sea ice will cause an overall decrease in the concentration of crude oil's denser and more polar constituents found towards the top of the ice, converse to the processes of evaporation and photo-oxidation, lowering the oil's dielectrics and potentially further decreasing the dielectrics of the oil-contaminated sea ice.

To better understand the impact of oil on sea ice dielectrics, an artificial oil-in-ice mesocosm experiment was designed, in which the physical migration of light-medium crude oil in first-year sea ice (e.g., percolation and migration through brine channels and ice cracks) as well as its chemical fractionation resulting of weathering processing tendencies, within, and below the sea ice were monitored. Specifically, this experiment features an oil spill from beneath young sea ice exposed to the weathering and transport processes of spreading, dispersion, evaporation, dissolution, and photo-oxidation in the presence of variable snow cover. Three hundred and thirty identified compounds were monitored spatially and temporally within the ice, water, and underlying snow. The changes made to the physical properties of both the oil and sea ice were investigated and the potential for remote sensing detection of oil in sea ice discussed. The purpose of the research addressed herein is to 1) build on the understanding of oil behavior in sea ice with an emphasis on microscopic changes and its impact on a macroscopic level; 2) help develop remote sensing methods for detecting oil in sea ice.

2. Materials and methods

The following subsections describe the conduction of the oil-in-ice mesocosm experiment; that is, the setup of the experiment apparatus and intended objectives, sampling and sample preparation procedures, instrumental methods and settings, processing of temperature, salinity, and volume profiles of the ice, and the associated theory behind quantum mechanical calculations used in this experiment as well as for the modelling of relative dielectrics (relative complex permittivity). This study focuses on changes made to the top ice (first 7.5 cm as opposed to the whole vertical cross-section) due to the limited penetration depth of interrogating microwaves (Firoozy et al., 2017) of radar.

2.1. Experiment apparatus and overview

An artificial oil-in-ice mesocosm experiment was conducted at the University of Manitoba (UofM) Sea-ice Environmental Research Facility (SERF) from January 15 to March 1, 2016. An open-ended 3 m diameter by 1 m deep insulated fiberglass tank with sampling ports built into its side at 10 cm intervals (vertically spaced) was used to facilitate the artificial oil-in-ice experiments (Fig. 1A) (Firoozy et al., 2017; Neusitzer et al., 2018). This test tank was customized and built by STRUCTURAL Composite Technologies Ltd. Winnipeg, MB. Initially, the fiberglass tank was filled with artificial seawater, derived from local source groundwater with the addition of sea salts (NaCl, MgCl₂, MgSO₄, CaCl₂, and NaBr), to a salinity of 32 parts per thousand (ppt). The tank was equipped with a heating coil, thermistor string, and temperature data logger. The thermocouple string, frozen into the ice, was used to measure the in-situ ice temperature profile at intervals of 2.5 cm, from top to bottom, every 15 min.

The experiment consisted of two phases, control and contaminated, over the period from January 15 to 21 and February 8 to March 1, 2016, respectively. However, the weather conditions (e.g., air temperature, snowfall) were different during the two phases (Fig. 2) (Neusitzer et al., 2018). To account for this difference, the SERF main pool (Fig. 1B) (Isleifson et al., 2014) was used as a secondary control for the duration of the experiment as a means of assessing the effect of the oil on ice temperature (see Sections 2.6 and 3.2 for details). Air temperature below 0 °C allowed ice growth for each phase (Fig. 2). During phase 1,

the sea ice grew to an approximate thickness of 30 cm and was subsequently melted to open water using a glycol heater and mixer (Fig. S1, Supplementary Section). During phase 2, once ice thickness reached approximately 6.5 cm, 20 L of a light-medium crude oil (Petroleum Crude Oil (Sour) from Tundra Oil & Gas Partnership) was injected into the water column from the tanks bottom midsection. The oil was then free to interact and migrate upwards through the sea water, sea ice, and potential snow cover.

2.2. Sampling and sample preparation

Sampling of sea ice was conducted during both phases of the experiment (Fig. S2, Supplementary Section). Over the course of the first phase, nine control ice cores were taken with a 9 cm diameter core barrel at distributed locations; on each of January 16 and 17 two cores were taken, and through January 18 to 22 individual cores were taken each day. Similarly, 17 contaminated ice cores were taken at various locations during phase 2; one core was taken on February 12, four on February 18 and 12 cores on March 1. Snow samples were also collected from each core site, before the retrieval of their respective ice core, where and when applicable. Additionally, on March 1, water samples (~600 mL each) at various depths were taken from the sampling ports (Fig. 1A), and surface water samples (~10 mL each) were retrieved at sites where contaminated cores were removed. In addition to the sampling of snow, sea ice and water, three field blanks (i.e., container with solvent free of any organic/inorganic substances that are to be tested in the real samples) were exposed to the atmosphere at the site in which one contained hexanes, another distilled water, and the last artificial sea water. Immediately after sampling, each ice core was sliced into three even sections (i.e., bottom, middle, and top) (an exception of two cores cut either in halves or quarters) with a sterilized steel saw (i.e., cleaned with hexane and mechanical force), before placement inside their own respective sterilized glass sample jars or sealable plastic sample bags and were subsequently vacuum sealed and placed in a freezer for storage to avoid sample degradation. All samples were then melted at room temperature before sample preparation and analysis.

Once melted, each of the snow, water, sectioned cores, and field blanks were measured volumetrically. For each sample, the crude oil was separated from the melted sea ice and snow using a separatory

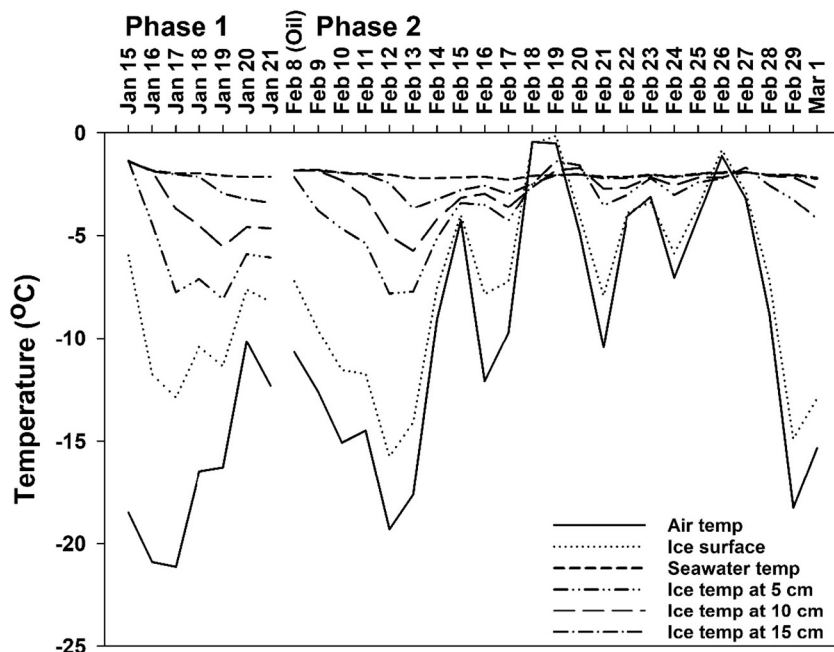


Fig. 2. Temporal profile of the recorded temperatures for a vertical cross section of the test tank (oil pool) pertaining to the water column, sea ice, and air above from January 15 to March 1, 2016. The break in the temperature profile from January 21 to February 8 pertains to the transition period between phases one and two.

funnel and hexanes (Fisher Scientific, Optima Grade) as solvent. Before separation, samples were spiked with deuterated polycyclic aromatic hydrocarbon (PAH) recovery standards (WELLINGTON LABORATORIES) and perdeuterated n-alkanes standards (Fisherbrand) to ascertain the associated losses through separation and subsequent volume reduction. The collected oil fractions were concentrated by fully reducing the solvent to dryness with the use of rotary and nitrogen evaporators. The remaining oil samples were then measured volumetrically. Additionally, three lab blanks (i.e., hexanes, distilled water, and artificial salt water) were prepared in the same manner.

2.3. Instrumental analysis by GCxGC-HR-TOF-MS

As crude oils contain thousands of hydrocarbons (HCs), each differing in chemical functionality, the use of analytical instruments capable of separating and quantifying highly complex mixtures are required. Prepared oil samples and blanks were diluted with Hexanes prior to analysis on a Pegasus multidimensional gas chromatography high resolution time of flight mass spectrometry (GCxGC-HR-TOF-MS, LECO) system using a one-dimensional setup with a RESTEK Rxi-PAH capillary column (60 m length, 0.25 mm internal diameter, 0.10 μm film thickness) and a carrier gas of nitrogen with a flow rate of 1.40 mL/min. The oven temperature was initially 80 °C, with an isotherm of 1.5 min, followed by a consequent temperature increase to 120 °C with a rate of 20 °C/min, then a further increase to 250 °C at 3 °C/min and finally, the GC oven temperature was programmed to 300 °C at a rate of 2 °C/min. The mass spectrometer conditions consisted of an electron energy of 70 eV, an ion source temperature of 300 °C, a mass range between 50 and 305 m/z , and an operational Time-Of-Flight (TOF) resolution of 25,000. Identification and quantification of the individual HCs were performed using parent PAH mix (CV calibration mix # 5, Restek), custom alkylated PAH mix (Restek), and n-alkane calibration mix (SPEX) recovery standards and the NIST standard reference data. Crude oil compounds which were not present in the standards were calculated against their closest compound from the standard with subsequent correction of their response factors. The values of the response factors were corrected through comparison of the used n-alkanes and PAHs standards with PAH Dibenzothiophene (and alkylated homologues) mixture (Chiron), mixture of 46 alkylated benzenes and PAHs (Chiron), Alkylbenzene mixture (Chiron), Alkylcycloalkane mixture 1 (Chiron), and Dibenzofuran (SPEX) recovery standards. Relative percentages of identified compounds were made based on their measured concentrations. Through the course of this experiment, the snow, ice, and water samples collected were analyzed for their resulting oil composition; that is, their alkane, cycloalkane, aromatic, and sulfur/oxygen heterocyclic content were mapped in order to observe the physical and chemical tendencies of the oil in ice and its effect on sea ice dielectrics. A full list of the investigated compounds (330), their target ions, which quantifier was used for quantification, and which quantifier was used for response factor correction (if applicable) can be found in the Supplementary Section (Table S1).

2.3.1. Quality assurance/control

Quality assurance was monitored in five ways. (1) The GCxGC-HR-TOF-MS system was tuned and validated before and after a sequence of standard/sample runs as well as between each set of 6–8 standards/samples. (2) Ten point standard curves were made from PAH and alkane standards yielding R^2 values of 0.99 for both PAHs and alkanes. (3) All measured analytes had a signal-to-noise ratio (S/N) greater than 6 and were interpolated within the range of generated standard curves (i.e., between 1.953 and 1000 ng/mL for aromatics and 9.765 to 5000 ng/mL for paraffinic compounds). (4) Lab and field blanks exhibited background solely (i.e., S/N < 3) when probing for the identified compounds of the oil with respective target ions. (5) Recovery yields could not be attained for the majority of samples due to the magnitude of oil found on average for the snow and ice samples (Ice –

9.2 mL; Snow – 3.8 mL) and the large dilution required for GC analysis. As a result, no corrections were applied to any of the measured concentrations. Based on methodology tests used to assess the losses associated with oil extraction and solvent reduction, all losses were found to be primarily attributed to nitrogen evaporation. However, due to the large film thickness of the reconstituted oil samples when placed inside a narrow vial upon nitrogen blow down, the overall evaporative loss was deemed insignificant as only the surficial oil was impacted. The exception to this is with regard to the sampled depth water samples which contained oil volumes less than 50 μL . This effect on the measured composition found in the water column is addressed in Section 3.1.1.

2.4. Analysis by infrared spectroscopy

Attenuated Total Reflection (ATR) Infrared Spectroscopy (IR) was used to qualitatively assess the effects of photo-oxidation for a subset of the prepared oil samples (i.e., one middle and top section from the February 12th core, three snow samples and two top ice core sections from February 18th core sites, and 12 top sections of the March 1st cores). A thin layer of each oil sample was placed directly on the ATR (Alpha-P, Bruker) diamond cell and was analyzed with a 2 cm^{-1} resolution over a 4000–374 cm^{-1} range. An air background subtraction was performed on all measured spectra. Due to the variance of the oil's thin films, the measured absorbance spectrum of each sample was scaled with respect to its largest absorbance value. Averaged IR spectra from contaminated ice (March 1st) and snow (February 18th) are presented in Section 3.2.3. The standard deviation of each respective data point is typically two orders of magnitude lower than their averaged scaled absorbance's. All individual IR spectra can be seen in the Supplementary Section (Figs. S3–S4).

2.5. Dielectric measurement: resonance perturbation method

Resonance Perturbation, a Cavity Perturbation Method presented in Chen et al. (2005), was used to measure the relative oil permittivities (dielectric constant) of 22 of the oil-contaminated ice core samples to determine any changes, due to weathering, from the initial technical mixture. The dimensions of the custom cavity (Gregory Bridges, Advanced RF Systems Lab) and samples used in the setup are ($W = 86 \text{ mm}$, $H = 43 \text{ mm}$, $L = 262 \text{ mm}$) and ($O/D = 2 \text{ mm}$, $I/D = 1 \text{ mm}$, $H = 43 \text{ mm}$) respectively. Schematics of the cavity and the samples can be seen in the Supplementary Section (Figs. S5–S6). Plots of the $|S_{11}|$ data (the electromagnetic reflection coefficient at the input to the cavity) for the resonant peak corresponding to the TE_{101} mode (frequency range 1.826–1.830 GHz) propagating within the cavity were constructed (e.g., Fig. S7, Supplementary Section). Relative permittivities for the weathered crude oil samples were calculated from their respective $|S_{11}|$ data using Eqs. (1)–(2).

$$\psi = [\sin(m\pi/2) \sin((p\pi/d) * 100 \text{ mm})]^2 \quad (1)$$

$$\epsilon'_r = (1 - 2)[(f_s - f_0)/f_0][V_C/4\psi V_s] \quad (2)$$

where π – mathematical constant; m and p – correspond to mode TE_{m0p} ; d – 262 mm; V_s – oil sample volume; V_C – resonant cavity volume; f_s – frequency of oil sample in glass tube at corresponding $|S_{11}|$ data minimum; f_0 – frequency of empty glass tube at corresponding $|S_{11}|$ data minimum. Eq. (1) provides ψ , a correction factor for TE_{m0p} modes, and Eq. (2) solves for ϵ'_r , the real component of relative complex permittivity.

2.5.1. Quality assurance/control

Precise measurements of the cavity and sample volume are required to calculate accurate relative permittivity values based on Eq. (2). Pyrex glass tubing was used for oil sample containment inside the resonant cavity. As manufactured tubing, drawn from molten glass, is not precise

and varies in wall thickness, its inner and outer diameters can fluctuate over a 1-meter span. Furthermore, minute changes in the glass wall thickness (e.g., 0.1 mm) can affect the degree of losses associated with measurement in the resonant cavity. To avoid inaccuracy in results due to inconsistency in glassware dimensions, each glass tube was measured twice, with and without its oil sample, assuring an exact response from the resonant cavity. Furthermore, manual measurements of the inner diameters of the glass tubes were also taken with an inverted light microscope (Leica DMIL LED) equipped with an ocular ruler with 0.01 mm spacing. The measured inner diameters of the glass tubes ranged from 0.93 to 1.05 mm. An assigned uncertainty of 0.02 mm in the ability to read the ocular ruler results in an uncertainty in the hundredths place of calculated permittivities. The calculated oil permittivities along with their measurement uncertainty are provided in Section 3.2.3.

2.6. Processing of temperature, salinity, and volume data

Bulk ice salinity of control and oil-contaminated samples were measured with a conductivity meter (Orion Star A212 – Thermo Scientific). Using total volumes (V_T), bulk salinities (S), and temperatures (T) measured for each respective ice core section, the respective brine volumes (V_B) were calculated using Eqs. (3)–(7) (Cox and Weeks, 1983; Leppäranta and Manninen, 1988).

$$D_i = 917 - 0.1404 * T \quad (3)$$

$$F_1 = -4.732 - 22.4 * T - 0.6397 * T^2 - 0.01074 * T^3 \quad (4)$$

$$F_2 = 0.08903 - 0.01763 * T - 5.33 * 10^{-4} * T^2 - 8.801 * 10^{-6} * T^3 \quad (5)$$

$$V_B/V = [(D_i/1000) * S]/[F_1(T) - (D_i/1000) * S * F_2(T)] \quad (6)$$

$$\%V_B = V_B/V * 100\% \quad (7)$$

where D_i – density of pure ice (kg/m^3); F_1 and F_2 – auxiliary functions; V_B/V – brine volume fraction; $\%V_B$ – percent brine volume; V_T (mL); S (ppt); T (°C).

The relative percentage of crude oil and its components found to be in the ice, water column, snow, and those found to have evaporated were calculated using Eqs. (8)–(10) based on the measured volume fractions and masses of the water, ice, and snow samples as well as the concentrations measured by GCxGC-HR-TOF-MS.

$$V_{\text{oil in the snow}} = V_{\text{oil in 1 ml of melted sample}} * \pi * R^2_{\text{pool}} * H * 0.777 \quad (8)$$

$$V_{\text{oil in the ice}} = V_{\text{oil in 1 ml of melted sample}} * \pi * R^2_{\text{pool}} * H * 0.92 \quad (9)$$

$$V_{\text{oil evaporated}} = V_{\text{oil injected}} - V_{\text{oil in the ice}} - V_{\text{oil dissolved}} - V_{\text{oil in the snow}} \quad (10)$$

where $V_{\text{oil in the snow}}$, $V_{\text{oil in the ice}}$, $V_{\text{oil evaporated}}$ – volume (mL) of oil present in the snow, ice, and which evaporated respectively. The volume of dissolved or emulsified oil in the water column was calculated by multiplying the volume of oil in 1 mL of water sample by the total volume of water in the pool taking into account the average ice thickness (18 cm). Similarly, the volume of oil migrated up into (or adhered under) the snow was calculated by use of Eq. (8) where H is the average snow thickness (1.9 cm), 0.777 is an average ratio between the density of the snow and water, R refers to the tank radius (1.5 m), and π is the mathematical constant. In the same manner, the amount of oil remaining in the ice was calculated using Eq. (9) where H is the average ice thickness of 18 cm, and 0.92 is an average ratio between the density of the ice and water. Lastly, evaporation loss was calculated using the simple approach of Eq. (10).

A simple, yet reasonably accurate, correlation (Eq. (11)) (Aboul-Seoud and Moharam, 1999), requiring specific gravity as the primary input was used to predict the thermal conductivities of the extracted oil's, from oil-contaminated ice core samples, to determine any changes in the thermal resistivity of the ice, due to changes in oil composition,

throughout the mentioned experiments. Specific gravity was calculated, using the measured densities of the oil samples and known density of water, at room temperature (294.150 K). The ambient room temperature of the lab, in which the oil masses were measured, was used as the respective input temperature.

An adapted expression for calculating the thermal conductivity of oil-contaminated sea ice (appropriate for First Year Ice) (Eqs. (11)–(13)) (Pringle et al., 2007; Montaron, 2012) was used to estimate the thermal conductivities of two contaminated phase ice cores (first 7.5 cm), both taken on February 18, 2016, differing significantly in their oil volume fractions, to assess the impact of oil magnitude on sea ice thermal conductivity. Note that the volume of oil by the oil pool thermocouple string was similar to that of the contaminated core consisting of a high volume fraction and the temperatures recorded at the sampling time were used as the input temperatures for this core, concerning Eq. (12). In contrast, the temperatures recorded from the main pool thermocouple string (secondary control) were used to formulate the input for the core with a very low oil volume fraction (rationale in Section 3.2.1).

$$k_{\text{oil}} = 2.540312(\gamma/\Theta)^{0.5} - 0.0144485 \quad (11)$$

$$k_{\text{sea ice}} = (D/D_i)(2.11 - 0.011 * T + 0.09(S/T)(D - D_i)/1000) \quad (12)$$

$$k_{\text{oil-in-ice}} = k_{\text{oil}} * (V_{\text{oil}}/V) + k_{\text{sea ice}} * (V_{\text{sea ice}}/V) \quad (13)$$

where k_{oil} (W/mK) – oil thermal conductivity; γ – specific gravity of the oil; Θ (K) – temperature; $k_{\text{sea ice}}$ (W/mK) – sea ice thermal conductivity; D_i (kg/m^3) – density of pure ice (Eq. (3)); D (kg/m^3) – density of sea ice (experimentally measured); S (ppt) – bulk salinity; T (°C) – temperature; $k_{\text{oil-in-ice}}$ (W/mK) – oil-contaminated sea ice thermal conductivity; V_{oil}/V – oil volume fraction; $V_{\text{sea ice}}/V$ – sea ice volume fraction.

2.7. Modelling of complex permittivity (dielectrics)

Dielectric profiles of contaminated top ice core sections were modeled using the Quasi Two-Phase Tinga-Voss-Blossey Mixture Model for contaminated sea ice as a four-phase mixture (TVB-4) given by Eq. (14) (Neusitzer et al., 2018; Firoozy et al., 2018) using the measured bulk salinities, temperatures, and volume fractions (ice, brine, oil, air) of the ice, and were modeled at 5.5 GHz. We performed model calculations at 5.5 GHz to coordinate with the center frequency of the polarimetric scatterometer system used during this experiment (Firoozy et al., 2017). This was done to compare the dielectrics of sea ice with low to high volume fractions of crude oil as well as to relate trends in dielectrics with other variables of interest. Note that ϵ_{ice} and ϵ_{brine} are calculated from temperature and bulk salinity measurements as described by Ulaby et al. (2014) and ϵ_{oil} was experimentally determined (Neusitzer et al., 2018).

$$\epsilon_{\text{mix}} = \epsilon_{\text{air,ice,oil}} + \frac{3v_{\text{brine}}\epsilon_{\text{air,ice,oil}}(\epsilon_{\text{brine}} - \epsilon_{\text{air,ice,oil}})}{2\epsilon_{\text{air,ice,oil}} + \epsilon_{\text{brine}} - v_{\text{brine}}(\epsilon_{\text{brine}} - \epsilon_{\text{air,ice,oil}})} \quad (14)$$

where ϵ_{mix} – modeled dielectrics of sea ice as 4-phase mixture; ϵ_{air} [5.5 GHz] – dielectrics of air ($1 - j0$); ϵ_{ice} [5.5 GHz] – dielectrics of pure ice (modeled); ϵ_{brine} [5.5 GHz] – dielectrics of brine (modeled); ϵ_{oil} [5.5 GHz] – dielectrics of crude oil ($2.2332 - j0.0373$) (experimentally measured).

2.8. Computational chemistry

A computational model was employed to simulate the effects of evaporation and dissolution through the calculation of the solubility of 189 compounds in salty water (seawater and melted sea ice) and their vapor pressures. Calculations for a representative subset of compounds found in the oil used for this experiment are provided in Table 1 and are used for qualitative support. A full set of calculations are provided in the Supplementary Section (Table S2). The liquid solute water

Table 1

Calculated salt water solubilities (mg/L) at -2.45°C and vapor pressures (bar) at -7.0225°C for a representative subset of compounds found in crude oil using ADF COSMO-RS.

Compounds	Solubility, mg/L	Vapor pressure, bar
Relatively soluble		
Naphthalene	117.50	0.0001
1-Methylnaphthalene	36.35	–
1-Ethylnaphthalene	9.77	–
1-n-Propylnaphthalene	2.75	–
1-n-Butylnaphthalene	0.67	–
1-n-Pentylnaphthalene	0.03	–
1-n-Hexylnaphthalene	0.14	–
n-Propylbenzene	26.25	0.0008
Tert-butylbenzene	19.95	0.0005
Dibenzofuran	27.28	–
Dibenzothiophene	16.22	–
Phenanthrene	10.90	–
Cyclohexane	63.78	0.0595
Relatively insoluble		
Octane	0.73	0.0080
Nonane	0.20	0.0023
Decane	0.04	0.0005
Undecane	0.01	0.0001
n-Butylcyclopentane	0.95	0.0013
n-Butylcyclohexane	0.35	0.0008

solubility (S_{water}), liquid solute vapor pressure (V_p), and the octanol/water partition coefficient ($\log K_{\text{ow}}$) for compounds of interest were computed with a popular implicit solvation model, ADF2016 COSMO-RS (COnductor like Screening MOdel for Realistic Solvents) (Klamt et al., 1998; Louwen et al., 2008; Pye and Ziegler, 1999). A geometry optimization was first performed using Amsterdam Density Functional (ADF) before executing the ADF COSMO calculation using the general parameter preset. The values obtained for V_p were calculated with respect to the average temperature measured at the air-ice interface during sampling while the values obtained for $\log K_{\text{ow}}$ and S_{water} were calculated with respect to the average temperature measured at the water-ice interface. The linear relationship between $\log K_{\text{ow}}$ and the Setschenow constant (K_{salt}) of a compound in a sodium chloride solution (Eq. (15)), formulated by Ni and Yalkowsky (2003), was used to calculate K_{salt} for each respective compound of interest. An alternative method for calculating K_{salt} with improved accuracy is proposed by Yu and Yu (2013). Use of $\log K_{\text{ow}}$ and S_{water} then allowed for calculating the solubility of a compound in sea water (S_{salt}) using the re-arranged empirical Setschenow formula, shown by Eq. (16), expressing the salting-out effect (Berkowitz et al., 2008). The salinity (mol/L) used in Eq. (16) was based on known values from measurements. The COSMO-SAC (Segmented Activity Coefficients) model (Xiong et al., 2014) can also be used to calculate partition coefficients and vapor pressures.

$$K_{\text{salt}} = 0.04 * \log K_{\text{ow}} + 0.114 \quad (15)$$

$$S_{\text{salt}} = S_{\text{water}} * 10^{-K_{\text{salt}} * \text{Salinity}} \quad (16)$$

where K_{salt} (L/mol); Salinity (mol/L); S_{water} (g/L); S_{salt} (g/L).

In order to assess the partitioning of the oil's composition within the ice, correlations derived from the measured concentrations (Section 2.3) of individual molecules and their various molecular properties (i.e., molecular volume, $\log K_{\text{ow}}$, molecular mass, V_p , and S_{water}) were used to assess the changes in oil composition spatially (i.e., vertical migration) and temporally within the ice as well as gauge the influence of these different properties. For this task, each measured concentration was scaled with respect to the total volume of its respective melted ice core sample (i.e., melted sea ice and oil). The relative percentage of each respective compound, found in a particular core, with respect to its own individual concentrations within the top, middle, and bottom sections of the ice were then plotted against their own respective molecular property. The molecular properties used in the correlations were

estimated using both EPI Suite 4.1 and Molinspiration Property Calculation Service (www.molinspiration.com). ChemDraw Prime 15.0 was used to draw the Lewis structures of each compound and their derived isomeric/canonical SMILES strings inputted into both EPI Suite and Molinspiration programs. The Modified Grain method, KOWWIN v. 1.68, and WATERNT models embedded in EPI Suite were used to estimate V_p (mm Hg), $\log K_{\text{ow}}$, and S_{water} (mg/L), respectively. Molecular volume (\AA^3) was estimated using Molinspiration.

2.8.1. Quality assurance/control

All compounds of interest were modeled as liquid solutes; as all compounds incorporated in an oil are dissolved in one another, compounds which would naturally be solid can be treated as a liquid in this context. The COSMO-RS theory and accuracy, including comparisons between other relevant methods, can be seen in the following hyperlink ([http://www.cosmologic.de/products/cosmtherm.html](http://www.cosmologic.de/products/cosmotherm.html)). COSMO-RS has proven to be the very best in predicting the physical properties of molecules compared to any other method used in industry; this is based on annual predictive modelling contests (A. Klamt, personal communication, 2018). Although, COSMO-RS has not been parameterized specifically for sub-zero temperatures, there are temperature-dependent interaction energy terms in COSMO-RS which are meant to capture the effect of increasing/decreasing the temperature. These adjustments work best if the system is within 50 K of standard temperature. As our calculated work herein has dealt with sub-zero temperatures warmer than -10°C , the accuracy is expected to be reasonable. Moreover, the relative accuracy is expected to be superior. As our work herein focuses on observing trends, relative accuracy is key.

2.9. Creation of contour plots

Contour maps of oil volume, snow thickness, sea ice dielectrics, brine volume fraction (%), and compound ratios were built using the modified Shepard's method in Surfer software. These plots are based on March 1st sample measurements addressed in the former subsections.

3. Results and discussion

The results shown in the following subsections were used to formulate an understanding of the oil-in-ice mechanics and to observe the extent of impact it had on the dielectrics of sea ice. The results demonstrate the link between chemical composition and physical properties.

3.1. Chemical composition

3.1.1. Dissolution of the crude oil

From the initial oil injection on February 8, at the tanks bottom center, to the last sampling date of March 1, 2.5% of the analyzed compounds were found to be dissolved in the water column (Table 2) (based solely on the polar constituents quantifiable by GC). The most abundant compounds found to be in the water are PAHs; in particular, naphthalene, methyl-, dimethyl-, and trimethylnaphthalenes. Naphthalenes are characterized by a relatively high solubility (Faksness et al., 2008), which decreases with the number of methyl groups or the length of alkyl chain (Table 1). This property is demonstrated by the compound ratio of 1,6-dimethylnaphthalene/1,3,6,7-tetramethylnaphthalene which is significantly higher in the water samples compared to the technical oil mixture, ice, and snow samples (Table 3). Amongst the alkylbenzenes, methylalkylbenzenes, and aryl isoprenoids, only low MW compounds (C_{13} – C_{19}) were present in the water column (Fig. 3). This is due to the lower solubilities of compounds containing longer alkyl chains (Table 1). Furthermore, the Aryl Isoprenoids Ratio (AIR) (Schwarz and Frimmel, 2004) C_{13} – C_{17} / C_{18} – C_{22} is almost 7 times higher in water than in the technical oil mixture (Table 3), clearly indicating a predominance of low MW compounds. The heteroaromatic

Table 2

Mass balance: estimated relative percentage of compounds which migrated in the snow, froze in the ice, dissolved in the water, and evaporated.

Compounds	Snow %	Ice %	Water %	Evaporation %	Sum %
Total	8.52	70.20	2.50	18.78	100
Alkanes (acyclic)	8.26	73.49	—	18.26	100
n-Alkylcyclopentanes	8.77	64.86	—	26.37	100
n-Alkylcyclohexanes	6.62	60.65	—	32.73	100
Methylalkylcyclohexanes	11.82	59.97	—	28.21	100
n-Alkylbenzenes	17.52	67.75	11.36	3.37	100
Methylalkylbenzenes	10.64	67.32	12.18	9.86	100
Aryl isoprenoids	8.27	64.95	13.73	13.05	100
PAHs	5.36	54.90	21.26	18.49	100
ΣNaphthalenes	4.11	54.42	27.65	13.82	100
Naphthalene	1.49	37.60	13.77	47.14	100
Methylnaphthalenes	1.75	41.76	28.43	28.05	100
Dimethylnaphthalenes	2.51	48.82	38.58	10.09	100
Trimethylnaphthalenes	4.21	56.91	27.76	11.11	100
Tetramethylnaphthalenes	7.22	60.81	8.44	23.52	100
Pentamethylnaphthalenes	9.37	63.96	1.48	25.20	100
Phenanthrene	13.59	74.94	10.28	14.79	100
Heteroaromatics	11.43	71.43	4.73	12.41	100

Where PAHs – polycyclic aromatic hydrocarbons.

Table 3

Relative chemical composition of technical oil mixture, and average composition of crude oil found in the snow, ice, and water in rel. % with respect to the technical mixture, snow, ice and water independently.

Compounds	Technical oil mixture	Snow	Ice	Water
Alkanes (acyclic)	74.69	70.64	77.04	—
n-Alkylcyclopentanes	2.56	3.97	2.74	—
n-Alkylcyclohexanes	3.34	2.13	2.58	—
Methyl alkylcyclohexanes	5.23	8.01	4.56	—
n-Alkylbenzenes	0.93	2.37	0.89	3.28
Methyl alkylbenzenes	3.36	4.79	3.28	13.78
Aryl isoprenoids	3.77	4.26	3.54	19.42
PAHs	4.93	2.45	4.28	58.88
Heteroaromatics	1.20	1.37	1.10	4.64
Sum, %	100	100	100	100
AIR	1.20	0.27	0.91	7.95
1,6-Dimethylnaphthalene/1,3,6,7-tetramethylnaphthalene	2.33	0.34	1.77	27.67

Where AIR – Aryl Isoprenoids Ratio: C13–C17/C18–C22 (Schwarz and Frimmel, 2004).

compounds dibenzothiophene, methyl-, dimethyldibenzothiophene, benzo(b)naphthothiophene, dibenzofuran, methyl-, dimethyldibenzothiophenes were identified and measured in crude oil. Unsubstituted dibenzothiophene and dibenzofuran represent the largest part of heteroaromatic compounds found in the water column due to their high solubility (Table 1). Aliphatic HCs such as alkanes, alkylcyclopentanes, and alkylcyclohexanes were not found in the water (Table 2), possibly due to the relatively small volumes sampled (600 mL) and potential losses associated with the rotary evaporators and nitrogen blow down (see Section 2.3.1).

Dibenzofuran and dibenzothiophene were present in 100% of the water samples. Both of these molecules are characterized by relatively low vapor pressures (Tables 1 and S1) and have molecular volumes and weights within 10% of one another (based on methods presented in Section 2.8). Based on the total sum concentration ratio of dibenzofuran to dibenzothiophene for 1 mL of a water sample, dibenzofuran was found to have an increased presence in the water column by a factor of 1.8, despite having one-third the concentration in the technical oil mixture. This result is primarily due to dibenzofuran having 1.7 times the salt water solubility of dibenzothiophene (Table 1). Similarly, dibenzofuran was present in the water column 3.2 times more than phenanthrene due to its higher solubility (2.5×) (Table 1). Similar trends were seen for other thermally stable aromatics.

Overall, the average (standard deviation) concentration of Total PAHs (i.e., the summation of parent and alkylated homologues) found in the water column was measured to be 48 (3) ng/mL. This value is close to the measured result of 40 (5) ng/mL found in Word et al. (2011) for the standard water accommodated fraction of Total PAHs. Moreover, the average concentration of naphthalene and phenanthrene found in the water column are 7 and 6 ng/mL respectively. These values are above the Canadian water quality guidelines for the protection of aquatic life (Canadian Council of Ministers of the Environment, 1999).

3.1.2. Chemical composition of the oil in ice

After being subjected to weathering processes, 70% of identified compounds remained in the ice (Table 2). Furthermore, partitioning of the oil due to evaporation and dissolution resulted in a change in the oil's composition in the ice relative to the technical oil mixture (Table 3). More specifically, the weathered oil lost most of its low MW and water-soluble compounds which can be seen by the decrease of the 1,6-Dimethylnaphthalene/1,3,6,7-Tetramethylnaphthalene and AIR in the ice samples compared to the initial technical mixture. Similarly, the same trend was seen with the composition of remnant PAHs in the ice, showing a correlation between concentration and alkylation degree (Table 2). Lighter compounds are more subjected to changes as they have relatively high solubilities and vapor pressures (Table 1). Furthermore, lower MW compounds are more mobile and have greater potential for upwards migration to the top of the ice, allowing for evaporation.

3.1.3. Chemical composition of the oil in snow

Snow cover contained 8.5% of the identified compounds (Table 2). Overall, the composition of the oil in the snow changed moderately relative to the technical oil mixture (Table 3) and all differences observed could be attributed to evaporation, as the snow surface interface was in direct contact with the air. Regarding alkylbenzenes, snow samples show a loss of low MW compounds in comparison to crude oil recovered from the ice (Fig. 3). Relative to the technical oil mixture, the percentages of alkylbenzenes, methylalkylbenzenes, alkylcyclopentanes, and methylalkylcyclohexanes in the snow are higher, which could be attributed to the lower vapor pressures of these compounds compared to their unalkylated analogues (Table 1). The percentage of alkylcyclohexanes in the snow relative to the technical mixture, however, does not follow the same trend. The observed AIR values for the snow samples are much lower in comparison to the ice cores, due to a greater interface area with the atmosphere, and technical oil mixture (Table 3) and could be attributed to evaporation.

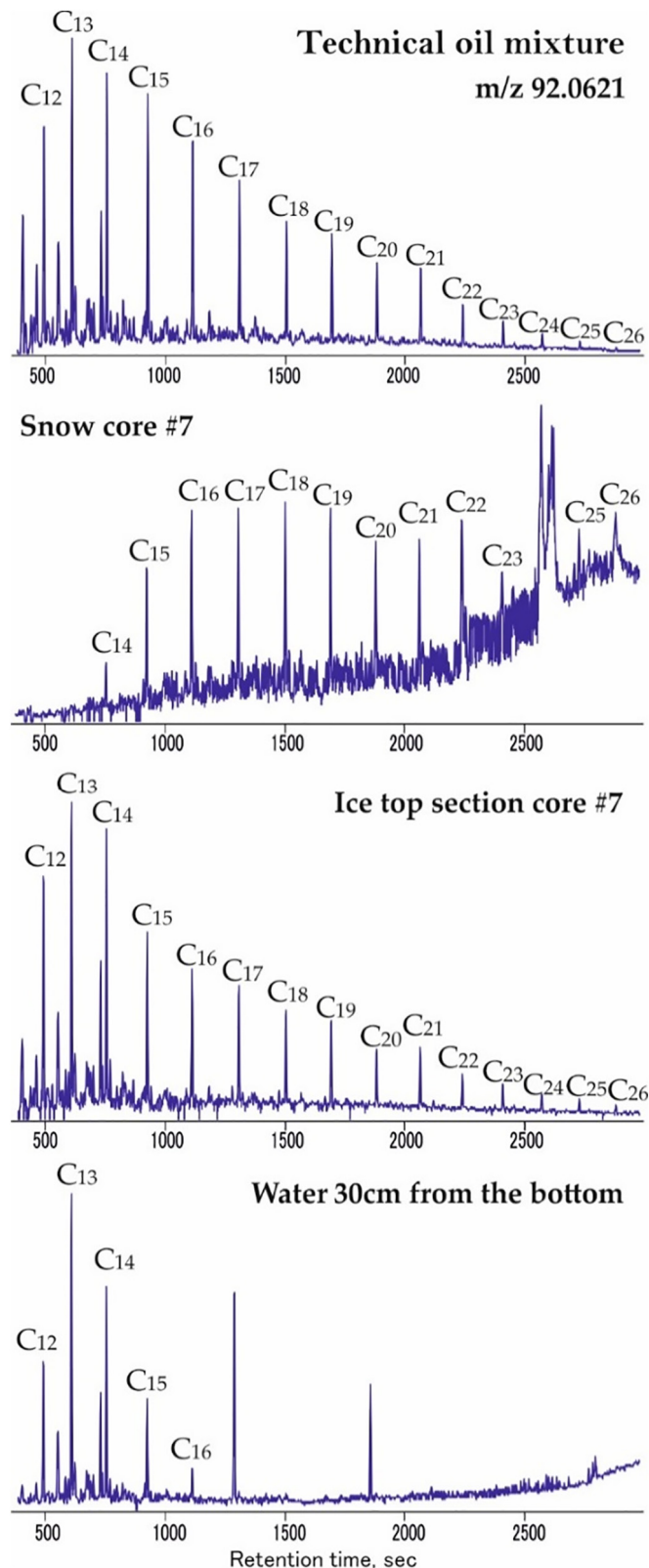


Fig. 3. Representative chromatograms of n-alkylbenzenes m/z 92.0621 obtained using GC-HR-TOF-MS.

3.1.4. Oil evaporation

In total, 18% of the identified compounds were found to have evaporated into the atmosphere (based on Eq. (10)). Aliphatic compounds – alkanes, alkylcyclohexanes, and alkylcyclopentanes are

characterized by the highest evaporation percentages (Table 2) due to their higher vapor pressures and lower solubilities (Table 1). Conversely, a lower evaporation percentage can be seen for the total PAHs due to their lower vapor pressures and higher solubilities, allowing for a greater tendency for dissolution. Contrary to the other PAHs, evaporation of unsubstituted naphthalene prevails despite its high solubility. This may be due to its higher vapor pressure, mobility (based on MW and size), and capability for migration up through the ice and subsequent evaporation before dissolution compared to larger PAHs. This hypothesis is supported by the low percentage of unsubstituted naphthalene remaining in the ice and snow which increases with the number of methyl substitutions; that is, an increasing number of methyl substitutions decreases the tendency to evaporate leading to more methyl substituted naphthalenes observed in the ice and snow (Table 2). Moreover, methyl-, dimethyl-, and trimethylnaphthalenes were observed to have higher dissolution resulting from their lower mobility, yet still relatively high solubility (Table 1). Tetra-and penta-methylnaphthalene were found in the water in relatively smaller amounts owing to their lower solubility. Similarly, the evaporative loss of alkylbenzenes was seen to be most significant for those with low molecular weights (Table 2, Fig. 3).

3.1.5. Partitioning within sea ice

In addition to external partitioning of the oil's composition, due to evaporation and dissolution, internal partitioning within the ice can also occur. Partitioning of molecules within sea ice likely depends on a variety of variables such as the length that the oil constituents must travel to reach the top of the ice, the diameter of brine channels, the shape and size of the molecules and their mass, volatility, and affinity for brine. Fig. 4 shows the vertically distributed concentration profiles (individual compounds) of a sampled core from the first sampling date (Feb. 12) and last sampling date (Mar. 1) plotted against their molar masses. Observation of the respective correlations shows a higher relative proportion of lower molecular weight (smaller and more volatile) components in the top part of the core which may reflect mobility and evaporative migration of these constituents up through the porous ice. On the other hand, the lower molecular weight (more water-soluble) constituents show a relative decrease near the bottom of the ice cores which presumably reflects dissolution and loss through brine channel drainage (Payne et al., 1991a). Furthermore, there is less separation (x-axis) between the top, middle, and bottom correlations seen for the March 1st core compared to the February 12th core. This increase in overlap is a result of temporal proximity/remoteness between the oil injection date (Feb. 8) and the two sampling dates (Feb. 12, Mar. 1). Much warmer ambient conditions followed after the first sampling date (Feb. 12–Feb. 27) (Fig. 2), allowing for equilibration and movement of compounds between the sections of the warmer ice. In contrast, the cooler ambient conditions seen between February 8th and 12th likely allowed for good separation (smaller brine channel diameters) and subsequent encapsulation. Specifically, during the subsequent warmer periods, the upper portions of the ice cores show a general decrease in the relative concentrations of intermediate molecular weight compounds while the most volatile constituents remain essentially constant. This could be due to brine channel drainage removing these moderately soluble constituents. At the same time the concentration of lower molecular weight constituents increases in the bottom section of the core also suggesting their vertical transport during brine channel drainage (Payne et al., 1991a).

In order to assess the influence of various properties (i.e., molecular volume, octanol-water partition coefficient, molecular mass, vapor pressure, water solubility) on the partitioning of oil-in-ice, linear or exponential regressions between these properties and the vertically distributed concentrations (e.g., Fig. 4) were calculated and tabulated in Table 4 for a subset of cores sampled throughout the experiment. Observation shows that the top and bottom section of the ice have the best associations, while the middle sections are either less significant or

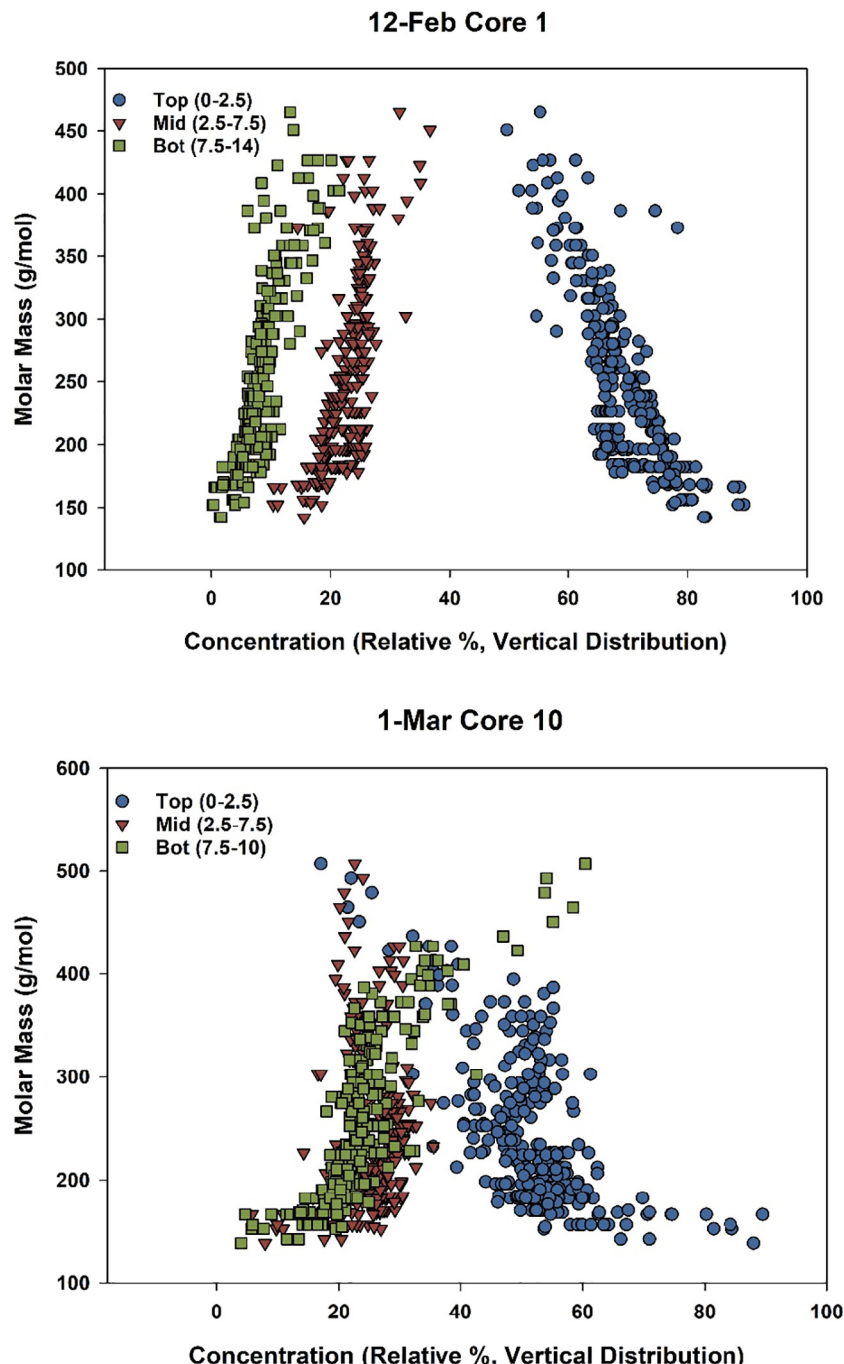


Fig. 4. Partitioning of the oil constituents found within the top, middle, and bottom sections of the ice.

neutral. This may be a result of migration distance traveled by the oil constituents with respect to ice thickness during oil injection (~ 6.5 cm). Overall, molecular mass and volume were found to have the best associations, followed closely by vapor pressure, the octanol-water partition coefficient, and water solubility last. Based on this, we speculate that molecular density would likely be the most prominent variable concerning partitioning. However, due to a lack of literature of the investigated compounds, a proper set of experimental densities could not be found. Similarly, their densities could not be derived theoretically due to a lack of experimental values required for their calculation (Density, 2016). We also speculate that water solubility showcased the weakest association, converse to vapor pressure, as oil is relatively insoluble and much more volatile. Further observation of Table 4 shows that the plotted trends deviate from linearity for cores sampled at later

dates. This can be seen from the scatter plots, pertaining to Table 4, provided in the Supplementary Section (Figs. S8–S13). As the ice warmed, the various groups of compounds which were monitored (i.e., PAHs, heterocyclic aromatics, acyclic alkanes, cycloalkanes, alkylbenzenes, aryl isoprenoids, steranes, terpenes, and tri-aromatic steranes) partitioned diversely within and from the sea ice. However, the aspect of partitioning is still visible in the correlations displayed in Figs. S8–S13. Last, it is worth pointing out that the weak to moderate associations found for these correlations are a product of the complexity and dynamics of oil and sea ice and still hold meaning within this context.

To further demonstrate how the sea ice partitioned the oil constituents, the relative acyclic alkane (n- and iso-alkane) composition found in the snow is plotted in Fig. 5 for a subset of snow samples taken from both the February and March sampling dates. As can be seen, each

Table 4Partitioning of crude oil: association strength (R^2) of various computed properties spatially and temporally.

Sample	Section	Regression type	V (A ³)	Log K _{ow}	MW (g/mol)	Ln Vp (mm Hg)	Ln Sw (mg/L)
12-Feb Core 1	Top (0–2.5 cm)	Linear	0.50	0.46	0.61	0.66	0.43
12-Feb Core 1	Mid (2.5–7.5 cm)	Linear	0.37	0.39	0.44	0.49	0.34
12-Feb Core 1	Bot (7.5–14 cm)	Linear	0.49	0.40	0.64	0.65	0.41
18-Feb Core 4	Top (0–7.5 cm)	Linear/Exp.	0.42	0.41	0.46	0.28	0.25
18-Feb Core 4	Mid (7.5–15 cm)	Linear/Exp.	0.09	0.09	0.08	0.02	0.01
18-Feb Core 4	Bot (15–22 cm)	Linear/Exp.	0.10	0.10	0.12	0.13	0.15
1-Mar Core 1	Top (0–2.5 cm)	Linear/Exp.	0.12	0.12	0.12	0.10	0.12
1-Mar Core 1	Mid (2.5–10 cm)	Linear/Exp.	0.25	0.21	0.35	0.45	0.26
1-Mar Core 1	Bot (10–11 cm)	Linear/Exp.	0.31	0.28	0.37	0.35	0.30
1-Mar Core 2	Top (0–5 cm)	Linear/Exp.	0.12	0.11	0.12	0.06	0.09
1-Mar Core 2	Mid (5–12.5 cm)	Linear/Exp.	0.01	0.01	0.00	0.02	0.01
1-Mar Core 2	Bot (12.5–19.8 cm)	Linear/Exp.	0.03	0.03	0.05	0.09	0.06
1-Mar Core 4	Top (0–5 cm)	Exponential	0.33	0.35	0.37	0.37	0.16
1-Mar Core 4	Mid-Top (5–10 cm)	Exponential	0.04	0.06	0.07	0.23	0.05
1-Mar Core 4	Mid-Bot (10–12.5 cm)	Exponential	0.04	0.02	0.07	0.12	0.01
1-Mar Core 4	Bot (12.5–18 cm)	Exponential	0.31	0.29	0.36	0.30	0.30
1-Mar Core 10	Top (0–2.5 cm)	Exponential	0.47	0.44	0.49	0.23	0.32
1-Mar Core 10	Mid (2.5–7.5 cm)	Exponential	0.02	0.02	0.03	0.17	0.03
1-Mar Core 10	Bot (7.5–10 cm)	Exponential	0.58	0.54	0.65	0.45	0.42
1-Mar Core 12	Top (0–10 cm)	Exponential	0.40	0.21	0.47	0.39	0.19
1-Mar Core 12	Bot (10–20.1 cm)	Exponential	0.23	0.21	0.27	0.24	0.19

Where MW – molecular weight (molar mass); V – molecular volume; K_{ow} – octanol-water partition coefficient; Vp – vapor pressure; Sw – water solubility; Linear/Exp. – both linear and exponential regression fits provide same associations.

sample exhibits a strong exponential correlation in which the highest concentrations (relative proportion) were found for the low molecular weight alkanes. This result was observed for samples of both low and high oil content. Furthermore, the relative acyclic alkane distribution found within the ice and snow sections of Core Site 4 (Feb. 18) (Fig. 5) shows an increasing hierarchy of oil magnitude towards the surface in which low molecular weight alkanes are concentrated; however, a slight deficiency of undecane (156 g/mol) and dodecane (170 g/mol) is seen in the snow relative to the top section , presumably reflecting an increased potential for evaporation at the air-snow interface. Similar trends were observed for the other core sites.

3.2. Changes in physical properties

3.2.1. Effect of oil on sea ice temperature, salinity, and dielectrics

A greater pension for upward migration rather than lateral

movement was exhibited by the oil causing a horizontal spatial heterogeneity of the oil-in-ice (Figs. 6A, 7A). Overall, the bulk of the oil throughout the pool migrated upwards to the top of the ice, through brine channels, air pockets, and any accessible cracks within the ice and via infiltration up through the sides of the tank emulating what might be observed in fractured ice (Fig. 1). The buoyancy exhibited by the oil is attributed to its relatively low density (< 1.0 g/mL for each sample, typically compared to the seawater and brine).

The presence of the oil on the surface and within the ice (Fig. 7A) was found to influence the temperature of the ice and snow significantly and can be attributed to an increase in the absorption of sunlight (decreased albedo) and the thermal insulating properties of the oil. From Fig. 6A; it can be seen that the snow is thicker near less contaminated areas where the concentration of oil is low and vice versa. Similarly, a relatively strong negative correlation ($R^2 = 0.75$) between ice thickness (vertical) of sampled contaminated ice and the oil

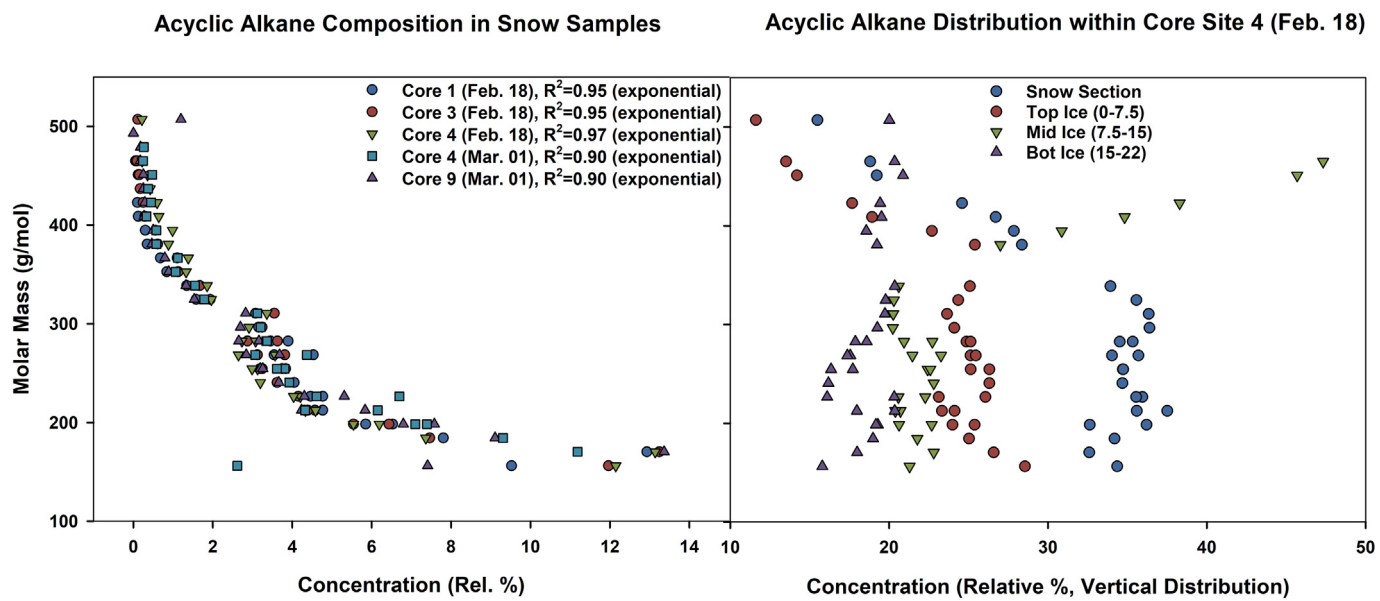


Fig. 5. Partitioning of the acyclic alkane constituents adhered beneath the snow.

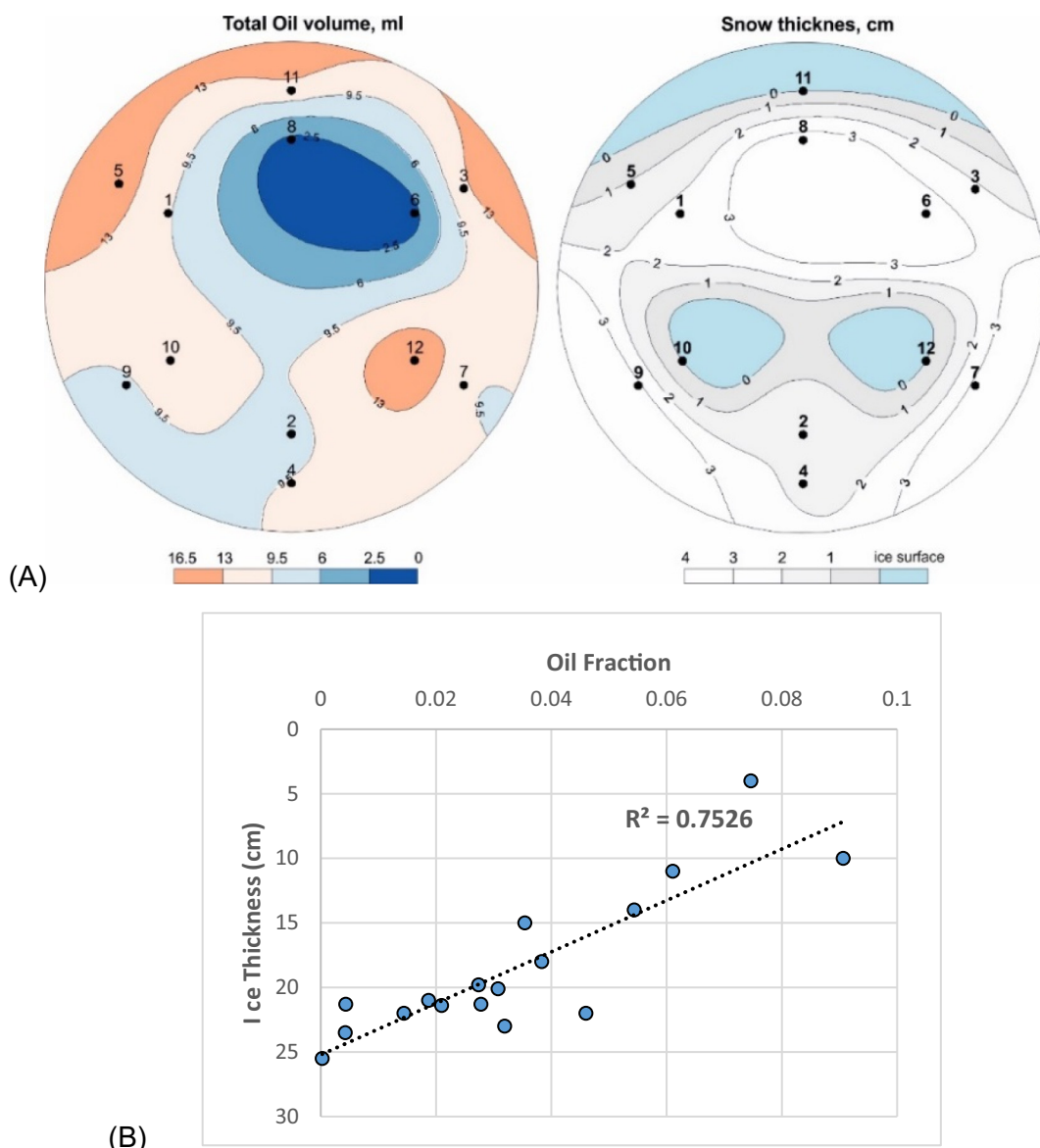


Fig. 6. A. Distribution of total oil volume in the ice (left) and snow thickness on top of the ice (right). The sampled March 1st cores are numbered and are represented by dots. The maps were built using the modified Shepard's method in Surfer software. B. Correlation between ice core thickness and oil volume fraction for all sampled oil-contaminated ice (February 8th–March 1st).

volume fraction contained within can be seen from Fig. 6B, suggesting a significant impedance of ice growth. From Fig. 7B it can be seen that the temperature profile of the ice (oil pool) was significantly warmer during the oil-contaminated phase (February to March) compared to its control (January). This temperature change could partly be due to the effect of crude oil on sea ice. However, as the ambient temperature was significantly warmer during the second phase of the experiment (Fig. 2), a proper assessment cannot be made based solely on Fig. 7B. Using the measured temperature profile of the secondary control (main pool) a reasonable comparison of ice temperature can be made between oil presence and lack thereof (Fig. 8). Three distinct differences between the two pools must be considered before making a valid comparison; (1) as the main pool contains a larger water body than the oil pool, it will have a longer temperature equilibration time; (2) due to differences in ice thickness, their temperature gradients will differ; and (3) the main pool is underground (warmer) while the oil pool is above ground (cooler). During a rapid cooling period (e.g., Feb. 27 to 29) (Fig. 2), the oil pool would undoubtedly be biased towards being colder than the main pool due to its smaller size and above ground location. Despite

this bias, an observed increase in the temperature of the oil pool can still be seen during fast cooling rates (e.g., Fig. 8). Furthermore, to minimize error resulting from differing temperature gradients between the oil and main pool, comparisons between their diurnal profiles (Figs. 8, S14) were restricted to the first 2.5 cm of ice.

From Fig. 8, a larger temperature discrepancy between both pools can be seen during the daytime compared to night owing to the absorption of sunlight by the oil (decreased sea ice albedo). Additionally, the presence of oil acted to reduce the thermal conductivity of the sea ice (Table 5). Based on the temperature discrepancy between both pools on Feb. 24 (end of cooling period on a date closest to Feb. 18) at Sunlight Peak (Fig. S14, Supplementary Section), an input temperature of +3.5 °C relative to the oil pool temperature was used to estimate the thermal conductivity of Core 2 relative to Core 4 (Feb. 18) shown in Table 5 (see Section 2.6 for details on calculation).

From Fig. 7C it can be seen that the salinity concentration of the ice (oil pool) was significantly lower during the contaminated phase of the experiment compared to the control period, especially at the top of the ice. A drop in salinity could be attributed to either or both of brine

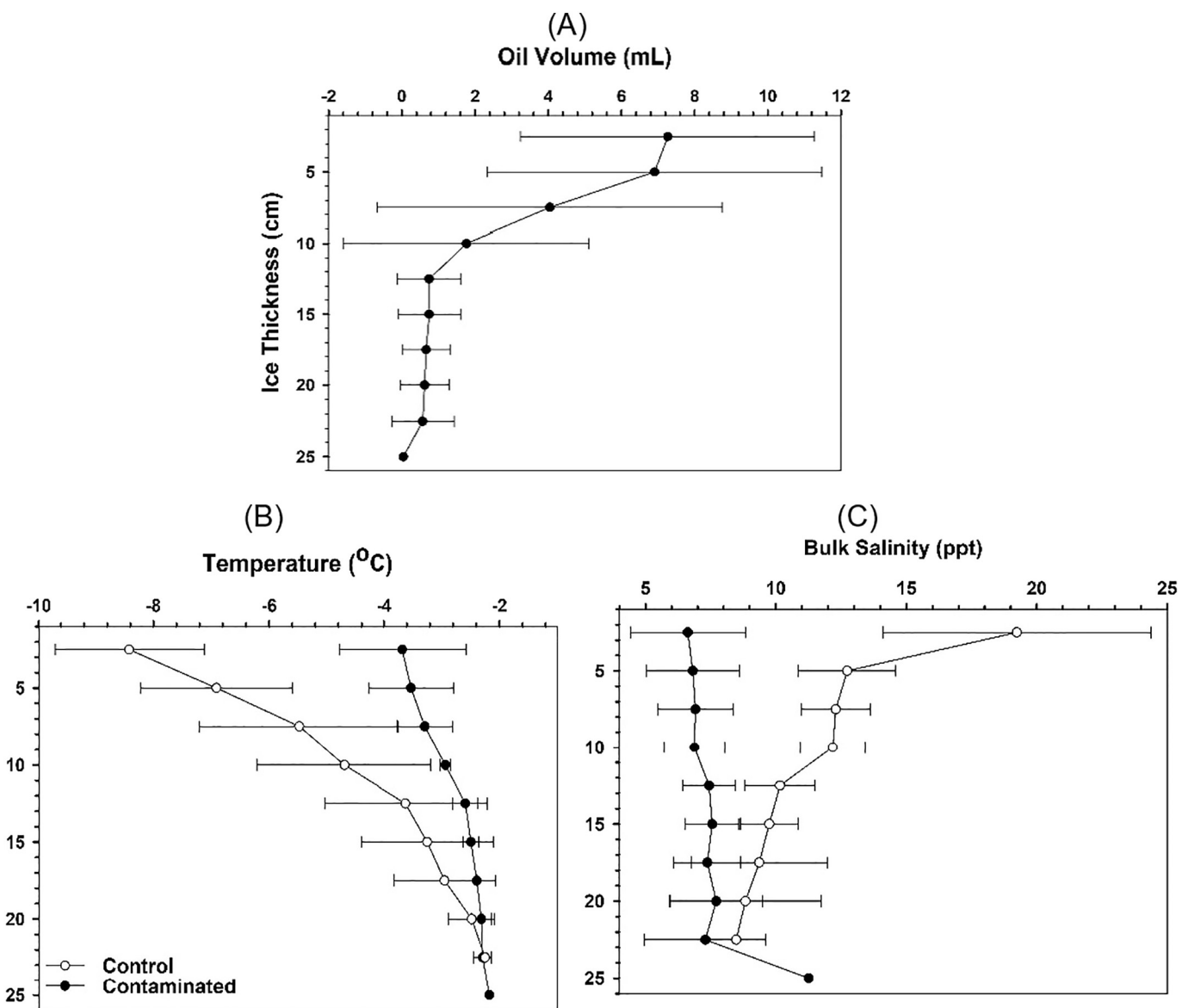


Fig. 7. Average oil volume (A), temperature (B), and bulk salinity (C) profiles for control ice (phase 1) and contaminated ice (phase 2) with standard deviation error bars.

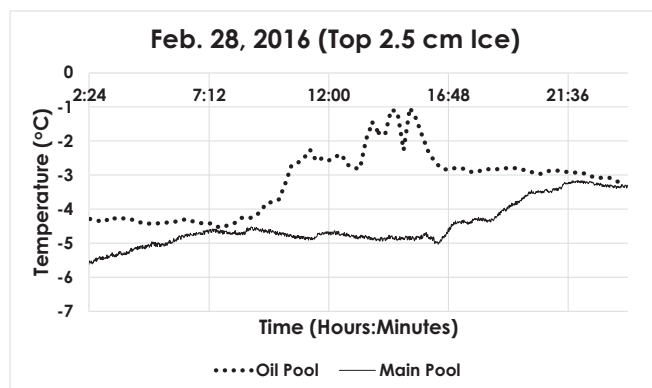


Fig. 8. Diurnal time series plots (Feb. 28) of the recorded temperature profiles for the first 2.5 cm of sea ice from both the oil pool and main pool (secondary control).

Table 5
Modeled sea ice thermal conductivity at daytime – sunlight peak hours.

	% V _{oil}	K _{oil-in-ice} (W/mK)
18-Feb Core 2	0.005	2.21 (D _{Melted})
18-Feb Core 4	3	1.91 (D _{Melted})
18-Feb Core 2	0.005	1.92 (D _{Solid})
18-Feb Core 4	3	1.77 (D _{Solid})

Where D_{Melted}/D_{Solid} – melted/solid sea ice density used in calculation; % V_{oil} – percent of crude oil in sea ice sample; K_{oil-in-ice} – thermal conductivity of the oil-contaminated sea ice.

expulsion from brine channels by replacement with oil and brine drainage due to the opening of brine channels owing to the rise in ice temperature. As brine salinity is a function of ice temperature, this desalination of the ice would also be partly due to the warmer ambient conditions. Due to the infiltration of oil from the sides of the pool as well as the magnitude of oil found in the ice, the potential for brine drainage would likely have been more significant than brine expulsion. This is supported by the moderately weak association ($R^2 = 0.46$)

Table 6

Linear regressions between modeled sea ice dielectrics, bulk salinity, and oil volume fraction of the top sections of the sampled sea ice.

Correlations	R^2 (linear)
$\text{Re}(\epsilon_r, \text{sea ice})$ vs. $\text{Im}(\epsilon_r, \text{sea ice})$	0.95
$\text{Re}(\epsilon_r, \text{sea ice})$ vs. Bulk S (ppt)	0.88
(V_{oil}/V) vs. Bulk S (ppt)	0.46

Where $\epsilon_r, \text{sea ice}$ – relative dielectrics of the sea ice; Re – real component; Im – imaginary component; Bulk S – bulk salinity of the sea ice; V_{oil}/V – oil volume fraction of the sea ice.

between the bulk salinity and oil volume fraction of the top sections of the sampled sea ice (Table 6). If brine expulsion were significant, a stronger association ($R^2 = 0.82$, Saltyukova et al., in prep) would be expected due to the systematic loss of salinity which occurs with increasing oil volume fraction.

The dielectric profile of the top of the ice shows a close correlation with % brine volume (brine fraction) (Fig. 9, Table 6) in which a drop in brine volume leads to a decrease in dielectrics. Assuming a greater brine volume corresponds to a greater amount of brine present (i.e., higher brine salinity, lower oil volume), the overall permittivity of the ice would be relatively high as the dielectric constant of brine ranges from approximately 52 to 45 at 5.5 GHz, corresponding to ice temperatures between -2 and -6 °C as seen by the contaminated ice (Figs. 2, 7B) (Fingas and Brown, 2007; Stogryn and Desargant, 1985). This result would then support our finding of reduced salinity due to oil presence.

Overall, the presence of oil-in-ice increased the temperature and lowered the salinity of the ice, thereby reducing its dielectrics. Initially, the experimentally determined sea ice dielectrics, at the upper few centimeters of the ice, before oil injection was $5.2 + 1i$ (Firoozy et al., 2017), which is higher than the modeled dielectrics of the oil-contaminated ice seen in Figs. 9 and 10. Similarly, the modeled magnitudes of the real and imaginary parts of the sea ice dielectric profile were found to be significantly higher, overall, during the control phase compared to the contaminated phase (Neusitzer et al., 2018). The effect of oil magnitude on sea ice dielectrics can be seen in Fig. 10 showing a steady decrease of the averaged dielectric profile with greater oil volume fractions. As previously pointed out, brine drainage is expected to be the primary cause of salinity loss. From Fig. 10, it is apparent that the most significant decrease seen for the average dielectric profile corresponds to the largest oil volume fraction (averaged). This result

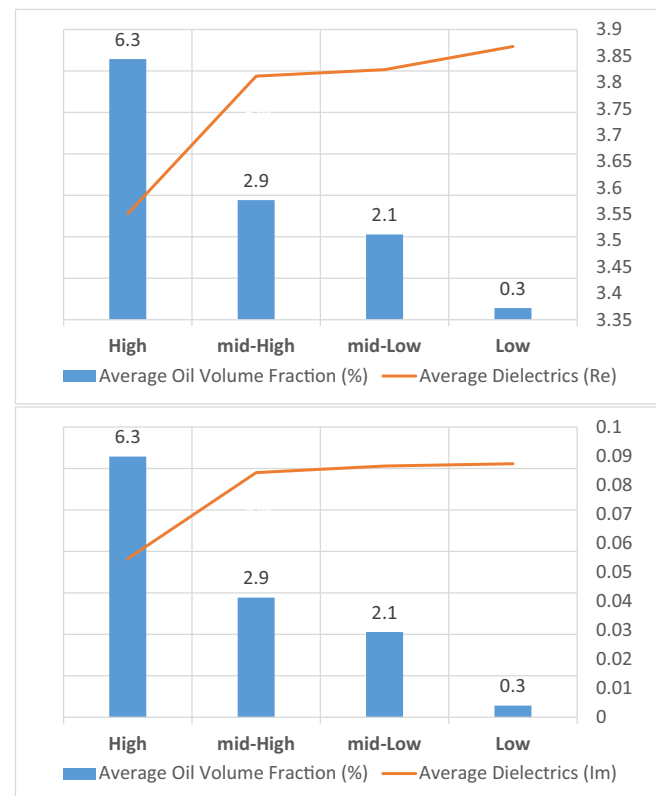


Fig. 10. Average modeled sea ice dielectrics (5.5 GHz) of the top sections of core samples with high to low oil volume fractions using the TVB-4 mixture model and concentration of crude oil in the ice.

can be attributed to a significant lowering of sea ice albedo which could only be established once a substantial oil volume fraction was met. Overall, the changes made to the dielectric profile of the ice, due to the presence of oil, resulted in a detectable shift in the radar signature of the ice (Firoozy et al., 2017). Specifically, in this experiment, we observed a 3 dB decrease of the normalized radar cross-section (NRCS) within 4 h of the oil introduction. As the noise associated with active radar has an uncertainty of 1 dB (Firoozy et al., 2017; Sharing Earth Observation Resources), this change is significant.

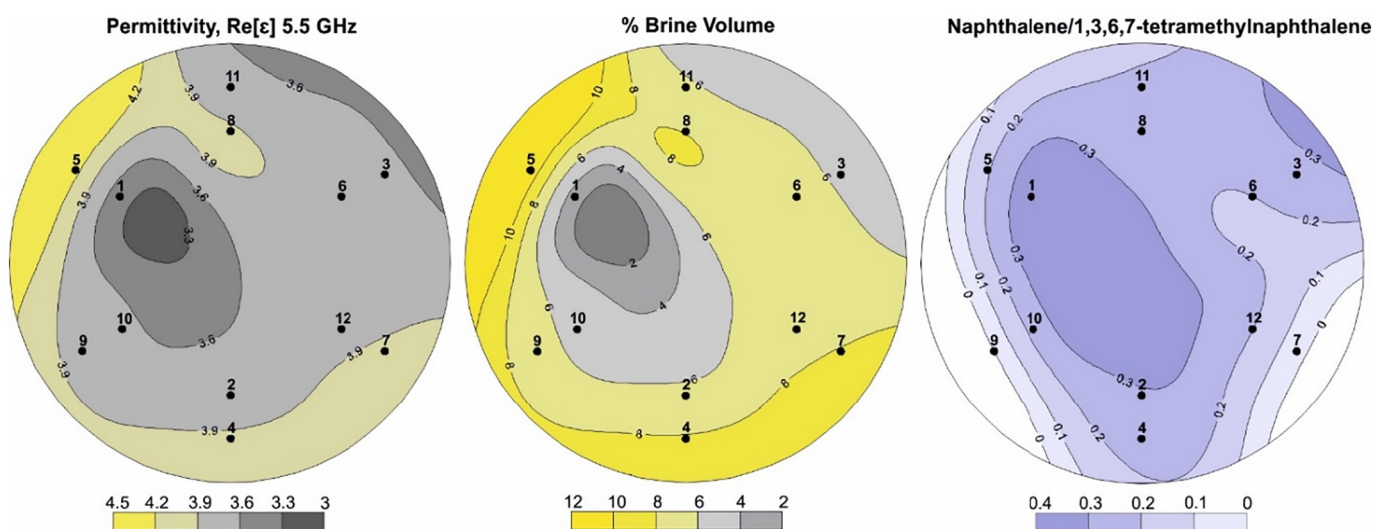


Fig. 9. The distribution of modeled relative permittivity (TVB-4), % brine volume, and naphthalene/1,3,6,7-tetramethylnaphthalene ratio in the top section of the ice. The March 1st core sites are marked with dots and bold numbers. The maps were built using the modified Shepard's method in Surfer software.

3.2.2. Degree of change on the density of oil due to weathering

Based on the results presented in [Section 3.1](#), internal partitioning of the oil's constituents within sea ice concentrates lighter compounds at the top of the ice and heavier compounds at the middle and bottom sections. Additionally, external partitioning via dissolution and evaporation reduce the more soluble and volatile components of the oil (e.g., aromatics as well as lower molecular weight alkanes, cycloalkanes, and PAHs). From literature, it is known that aromatics typically have larger densities than paraffins (i.e., alkanes and cycloalkanes), that the densities of n-alkanes as well as alky cyclopentanes and alkyl cyclohexanes increase with chain length, and that the densities of alkyl benzenes and alkyl naphthalene's decrease with chain length ([The Engineering Toolbox, 2017](#); Chemical databases: ChemSynthesis, PubChem, ChemSpider, LookChem, NIST).

The overall density of a complex mixture can be described by a summation of its individual densities which are weighted by their mass fractions similar to a weighted average ([Density, 2016](#)). Therefore the density of the oil within the snow, top, middle, and bottom sections of the ice can be described by their overall change in chemical composition. Furthermore, the oil of interest is composed of ~75% acyclic alkanes ([Table 3](#)) and so changes which target the n- and iso-alkanes may predominate. Lastly, as the oil was either encapsulated within ice or adhered underneath snow, the effects of evaporation may have been weakened and dissolution processes more significant; although this cannot be completely substantiated as a thorough investigation into the polar fraction was not conducted herein. However, the polar fraction of the oil and its evolution in sea ice will be investigated in future work with the use of ATR-IR and multidimensional liquid chromatography high resolution time of flight mass spectrometry (LCxLC-HR-TOF-MS).

Overall, the average oil densities found for the technical mixture, snow, top, middle, and bottom portions of the ice are 0.90, 0.76, 0.84, 0.88, and 0.78 g/mL respectively. Unlike warm marine conditions which consistently act to increase the overall density ([National Academies of Sciences, 2016](#); [Brandvik et al., 2006](#); [Afenyo et al., 2016b](#); [Payne et al., 1991b](#)), there is potential for decreases within sea ice. Note that the technical mixture was found to have traces of incorporated water (microscale emulsification) unobservable to the human eye. This was verified through the use of ATR-IR in which the IR spectrum of the technical mixture exhibited rotational bands associated with water vapor ([Fig. S4, Supplementary Section](#)). Unlike the technical mixture, most of the reconstituted oil extracts did not show evidence of water incorporation, as a result of the sample preparation detailed in [Section 2.2](#). Consequently, it is expected that the unaltered weathered samples would have been moderately higher in density and permittivity relative to the technical mixture.

3.2.3. Degree of change on the permittivity of oil due to weathering

Overall, 22 crude oil samples were measured for their relative permittivities (dielectric constants); 14 samples derived from top ice core sections, four from snow samples taken from respective core sites, three from the middle of ice core sections, and only one from a bottom ice core section due to insufficient oil required for the permittivity measurements. After being subjected to weathering processes, the permittivities for most of the measured samples became lower than the original technical mixture (2.25) and ranged from 1.81 to 2.30 ([Table 7](#)). The observed decrease in oil permittivity can be attributed to the weathering processes of dissolution and internal partitioning within sea ice which acted to concentrate the less dense (less polarizable) components of the oil, thereby lowering its electrical and thermal conductivity ([Table 8](#)) ([Aboul-Seoud and Moharam, 1999](#); [Elam et al., 1989](#); [Panuganti et al., 2016](#); [Van Dyck et al., 2017](#)). Furthermore, the presence of snow cover through the experiment (photos provided in [Supplementary Section, Fig. S15](#)) diminished the effect of photo-oxidation of the oil-in-ice and oil adhered beneath snow. Unlike dissolution and internal partitioning processes, photo-oxidation would act to increase the density and polarity of the oil through photochemical

Table 7

Permittivity (Re) measurements of February and March snow and ice samples at frequency range TE₁₀₁ (1.826–1.830 GHz).

Samples	Core #	Section	Re(ϵ_r , oil)
1-Mar	10	Top	1.81(3)
18-Feb	1	Snow	1.83(4)
1-Mar	12	Top	1.87(4)
18-Feb	4	Top	1.95(4)
18-Feb	3	Top	1.98(4)
1-Mar	9	Top	1.99(4)
1-Mar	5	Top	2.01(4)
18-Feb	3	Snow	2.03(5)
18-Feb	4	Snow	2.05(4)
1-Mar	9	Snow	2.06(4)
1-Mar	10	Mid	2.08(5)
18-Feb	4	Bot	2.08(4)
1-Mar	1	Top	2.11(5)
1-Mar	11	Top	2.14(5)
18-Feb	1	Top	2.15(5)
1-Mar	4	Top	2.16(5)
18-Feb	4	Mid	2.17(5)
12-Feb	1	Top	2.19(5)
1-Mar	3	Top	2.21(5)
Technical oil mixture			2.25(5)
1-Mar	1	Mid	2.26(5)
1-Mar	7	Top	2.28(6)
1-Mar	2	Top	2.30(6)
Average snow-section			1.99
Average top-section			2.08
Average mid-section			2.17
Bottom-section			2.08

Table 8

Association between the averaged relative permittivities and modeled thermal conductivities of oil derived from the top, middle, and bottom sections of the sampled sea ice.

Crude oil	Re(ϵ_r , oil)	K _{oil} (mW/mK)	D _{oil} (g/mL)
Technical mixture	2.25	126	0.90
Average snow section	1.99	115	0.76
Average top section	2.08	121	0.84
Average mid-section	2.17	124	0.88
Average bottom section	2.08	117	0.78
R ² (linear)	0.89		

Where Re(ϵ_r , oil) – real component of the relative complex permittivity (dielectrics) of oil (i.e., oil dielectric constant); K_{oil} – thermal conductivity of oil; D_{oil} – oil density.

Averaged IR Spectra of Crude Oil Samples

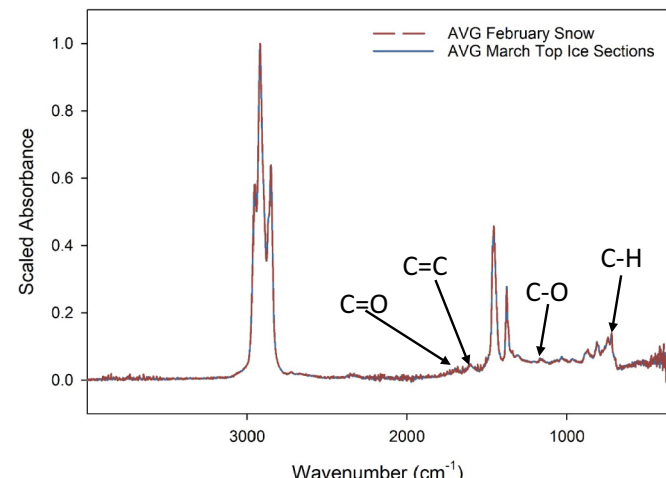


Fig. 11. Averaged infrared spectra of oil samples derived from top sections of sampled ice from March 1st and snow samples taken February 18.

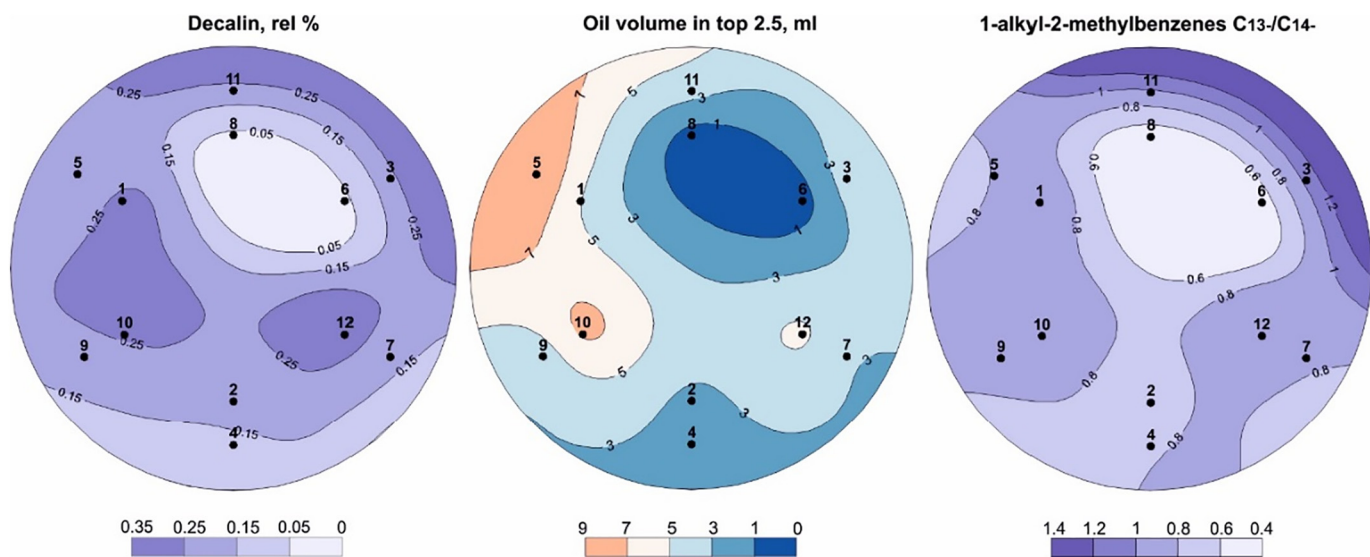


Fig. 12. Maps of distribution of decalin, 1-alkyl-2-methylbenzenes C_{13}/C_{14} ratio and oil volume in the top 2.5 cm of the March 1st samples.

transformations. A lack of increase in the IR absorbance bands associated with photo-oxidation (e.g., $C=O$ at $\sim 1774\text{ cm}^{-1}$, $C=C$ at $\sim 1600\text{ cm}^{-1}$, and $C-O$ at $\sim 1250\text{ cm}^{-1}$) can be seen from the IR spectra of the February and March oil samples (Fig. 11) compared to the technical oil mixture (Fig. S4, Supplementary Section and Stout and Wang, 2016; Fresco-Rivera et al., 2007; Saltymakova et al., in prep, Fig. S16). The difference in permittivity from sample to sample is a result of weathering susceptibility. On average, the oil found in the snow had the lowest permittivity (1.99), followed by the top and bottom sections of the ice (2.08). The mid-section of the ice was found to have the highest permittivity (2.17). These values are in agreement with the changes in oil composition discussed in Section 3.1 in which the more hydrophilic and dense compounds of the oil (e.g., aromatic and heterocyclic) were depleted in the snow and at the top and bottom sections of the ice due to dissolution processes, and internal partitioning reduced the concentration of the heavier (denser) compounds (e.g., high molecular weight alkanes) found towards the top of the ice and adhered beneath the snow. Furthermore, on an individual core basis (i.e., cores 1, 3, and 4, Feb. 18/16; cores 1, 9, and 10, Mar. 1/16), a similar trend is seen in which middle sections have the highest oil permittivity, followed by their bottom, top, and snow sections. Exceptions to this can be seen for Cores 3 and 4 in which their snow sections have slightly higher permittivities than their top sections (possibly owing to a marginal degree of photo-oxidation).

These values given for the weathered oil permittivities vary considerably and will act to directly lower the overall dielectrics of sea ice when taken as a system (i.e., ice, brine, air, and oil). More so, a change in the oil's permittivity and thermal conductivity, brought on by its change in composition (Table 8) can have an indirect influence on the physical properties of sea ice. For example, a lowered thermal conductivity (improved thermal insulator) would result in a greater temperature gradient from the seawater interface to the atmosphere, and consequently, a different temperature profile from a region of uncontaminated sea ice (Desmond, 2018). Additionally, changes in the oil's composition would affect oil density, buoyancy, and viscosity influencing its movement in the Arctic environment which would, in turn, impact the salinity of the ice and potential for remote detection.

3.3. Chemical migration and tendencies of soluble components

Determination of patterns and relationships seen in this section were conducted by comparison of Spearman's rank correlation coefficient. Observation of Fig. 9 shows a negative correlation between %

brine volume and the compound ratio of Naphthalene/1,3,6,7-tetramethylnaphthalene; that is, as the brine volume decreases towards the ice surface, an increase in this compound ratio can be seen at the top of the ice. In other words, the areas in which the brine volume is smaller, the percentage of lighter and more water soluble components is greater, possibly owing to their increased upwards mobility and smaller size, allowing them to permeate through narrower channels. This increase in Naphthalene/1,3,6,7-tetramethylnaphthalene at higher brine concentrations may also reflect the salting-out effect (Berkowitz et al., 2008) of the higher alkylated component (Saltymakova et al., in prep). In contrast, when the brine volume is larger, a lower percentage of lighter and more water-soluble components can be found at the top of the ice, possibly due to increased dissolution of lower molecular weight constituents from the surface to the water column below via brine channel drainage (Payne et al., 1991a). At elevated temperatures, expansion of brine channels allows for the increased dissolution of lighter and more soluble components such as PAHs. As PAHs dissolve in the brine and water formed due to melting of the ice, they are flushed out through the open brine channels and air pockets. Confirmation of this hypothesis can be seen by the presence of light PAHs and alkylbenzenes in the water column (Fig. 3, Tables 2 and 3).

This phenomenon is also illustrated by the agreement between decalin, the ratio of 1-alkyl-2-methylbenzenes C_{13}/C_{14} and the amount of oil in the top ice section (Fig. 12). Both decalin and 1-alkyl-2-methylbenzenes are found in the water column (Tables 2 and 3) and their ability to dissolve is proportional to the interface area between the oil components and brine. Therefore, increased contact between the oil and brine within the ice will allow for larger amounts of the water-soluble components to dissolve and migrate downwards into the water column (Payne et al., 1991b). Consequently, if the oil concentration is relatively small, dissolution quickens due to fewer internal interactions of oil components and more external interactions with the solvent. As such, areas that have smaller amounts of crude oil show a deficiency of water-soluble components.

3.4. Conclusion

This paper presented a case study on the behavior of crude oil in a sea ice environment to observe the changes made to the oils composition and the resultant effect it had on the physical properties of the ice, and more specifically on sea ice dielectrics. For this purpose, oil was injected underneath the young sea ice and was sampled over a three-week time span.

Immediately, upon oil injection, the chemical composition of the oil started to change due to the dissolution of water soluble components and the evaporation of volatile components. The resultant percent of dissolved compounds found in the water column is relatively high, comparative to an open water scenario, due to the presence of ice cover, which hindered the evaporation of volatile components. As a result, 2.5% of the identified HCs and heterocyclic compounds were dissolved, mostly within light PAHs, low MW alkylbenzenes and aryl isoprenoids, enabled by their higher solubilities. Evaporation also significantly modified the oils composition and led to a loss of almost 19% HCs, including some of the more water soluble compounds, despite the presence of the ice. It is speculated that this effect was caused by the high mobility of unsubstituted compounds, allowing for the potential of surface penetration to the surface and subsequent evaporation over dissolution into the water column. Overall, 70.2% of the identified HCs were found in the ice and 8.52% in the snow and their composition indicates a lower percentage of PAHs, alkylcyclohexanes, and alkylcyclopentanes compared to the original technical oil mixture. These changes were caused by both high dissolution and evaporation, which eliminated the lighter compounds. Additionally, snow lost more volatile components due to its greater interface area with the atmosphere.

During the experiment, oil penetrated to the surface of the ice causing melting of the overlying snow. It was observed that the volume of the snow remaining on top of the ice was inversely related to the total volume of the oil content found in the investigated area. Similarly, impedance of ice growth was found to be increased in areas with higher oil volume fractions. This was most likely due to the oils ability to absorb sunlight energy, consequently reducing the albedo of the ice, thereby increasing the temperature of the surrounding area. Furthermore, this rise in temperature could have caused an opening of the brine channels, pushing brine out into the water. This brine volume reduction led to a recession in the permittivity of sea ice, and this change was impacted to a larger degree with greater amounts of oil present.

Due to the ice melting caused by increases in temperature, light PAHs dissolved in the formed water and were subsequently flushed out through opened brine channels and air pockets. This phenomenon is illustrated by (1) the close inverse correlation between brine volume and the percentage of light PAHs, (2) the light PAHs present in the water column, and (3) the connection between the relative percentage of water-soluble compounds and the volume of the oil present in the ice. The ability to dissolve oil components in melted sea ice could be considered as a function of interface interaction between oil components and solvent brine, which increases with lowered amounts of oil in the ice.

Overall, these changes led to a noticeable decrease in sea ice dielectrics, mainly through a change in the sea ice temperature and salinity, which can be potentially detectable by remote sensors. Additionally, changes in the oils chemical composition, due to weathering, showed potential for further influencing the physical properties of the ice, augmenting the movement tendencies of oil as well as its permittivity, thermal conductivity, and density. The processes of dissolution and partitioning within sea ice were primarily responsible for lowering the density, permittivity, and thermal conductivity of the oil, which would further impact the physical properties of the ice. These compositional changes due to competing weathering processes have the potential for both positive and negative feedback loops of the overall sea ice permittivity, taken as a whole system (i.e., ice, brine, air, and oil).

3.4.1. Future work and outlook to a real world oil spill scenario

While sea ice dielectrics are not directly measured with remote sensing technologies, they are a governing factor of microwave interactions. Generally speaking, the brine volume fraction has the highest impact on the NRCS of the sea ice and consequently, the incorporation of oil in sea ice has a significant influence on the NRCS, as it has the

potential to displace brine.

In a real world scenario, radar can be used in low visibility conditions (e.g., darkness, blowing snow, rain and fog) to detect oil-in-ice. This technique is however surficial and is limited to probing underneath snow and approximately the first 8 cm of ice (Puestow et al., 2013). Consequently, this technique is dependent on oil migration to the surface (e.g., in spring) (Oggier, 2014) and resultant displacement of brine and would not be as applicable to an older, less permeable, and less saline ice type. However, in the Northern Arctic, an oil spill is likely to occur during the early stages of freeze-up when the industrial and shipping activity is most heightened. The presence of oil between ice floes or within the top portions of the ice, where it can be potentially detected by this method, is a likely scenario.

As the density, thermal conductivity, and albedo of different oil types (e.g., diesel fuel, light crude, heavy crude, heavy fuel) differ, their rate of migration to the surface and their impact on sea ice brine would likely be distinguishable. Consequently, it would be possible to differentiate between a lighter and heavier oil by the extent and slope of the gradient observed for the NRCS pre- and post-oil introduction (e.g., Firoozy et al., 2017). However, continual monitoring (e.g., every few hours) would be required to establish a reliable gradient. Another potential method to infer the composition of the oil (i.e., light, medium, heavy) using radar would be to utilize an inversion algorithm to ascertain the permittivity of the oil (Desmond et al., 2018; Firoozy et al., 2018; Firoozy et al., 2017; Firoozy et al., 2015; Firoozy, 2015). As it was established herein, there exists a correlation between oil density and permittivity (Table 8) which could be exploited.

Future work will investigate the potential of using radar for interrogating the composition of crude oil (i.e., light, medium, or heavy) based on a distinct contrast in the dielectric profile. Ultimately, being able to ascertain the whereabouts and state of the oil-in-ice will allow for the correct mitigation response dispatch, as the potential for various mitigation procedures (e.g., bio-remediation and in-situ burning) depend on the location and composition of the oil inside the sea ice.

Acknowledgements

Canada Research Chairs (CRC) programs, Natural Sciences and Engineering Research Council of Canada (NSERC), the Canada Foundation for Innovation (CFI) and the University of Manitoba, Canada. We thank Dave Babb (Research Scientist, CEOS) and Dave Binne (SERF Technician, CEOS) for their kind help throughout the SERF experiment. We also thank Alexis Burt (Technician, CEOS), Debbie Armstrong (Technician, CEOS), and Emmelia Wiley (Technician, CEOS) for their assistance in acquiring necessary supplies used during the experiment. Last, we thank Jake Ritchie (Technician, CEOS), James Xidos (Dept. of Chem., UofM), Gregory Bridges (Advanced RF Systems Lab, Dept. of Elec. & Comp. Eng., UofM), Puyan Mojabi (Dept. of Elec. And Comp. Eng., UofM), and Lesa Cafferty (Cafferty's Scientific Glassblowing) for their assistance with the project analyses. This work was supported by and is a contribution to the ArcticNet Networks of Centres of Excellence and the Arctic Science Partnership (ASP), as well as Genome Canada and Microbial Genomics for Oil Spill Preparedness in the Canadian Arctic (GENICE).

Appendix A. Supplementary data

Supplementary data to this article can be found online at <https://doi.org/10.1016/j.marpolbul.2019.03.021>.

References

- Aboul-Seoud, A., Moharam, H.M., 1999. A simple thermal conductivity-temperature correlation for undefined petroleum and coal liquid fractions. *Institution of Chemical Engineers Trans IChemE* 77, 248–252.
- Afenyo, M., Khan, F., Veitch, B., Yang, M., 2016a. Modeling oil weathering and transport

in sea ice. *Mar. Pollut. Bull.* 107, 206–215.

Afenyo, M., Veitch, B., Khan, F., 2016b. A state-of-the-art review of fate and transport of oil spills in open and ice-covered water. *Ocean Eng.* 119, 233–248.

AMAP, 2010. Assessment 2007: Oil and Gas Activities in the Arctic—Effects and Potential Effects. vol. 1.

Anderson, J.W., Neff, J.M., Anderson, J.W., Hightower, G.M., 1974. Characteristics of dispersions and water-soluble extracts of crude and refined oils and their toxicity to estuarine crustaceans and fish. *Mar. Biol.* 27 (1), 75–88.

Density. In: API Technical Data Book, 10th ed. The American Petroleum Institute and EPCon International.

Ballesteros, H., Magdol, Z., 2011. Biodegradation of polycyclic aromatic hydrocarbons in simulated Arctic Sea ice brine channels and protistan predation. In: International Oil Spill Conference Proceedings (IOSC). vol. 2011 American Petroleum Institute No. 1.

Berkowitz, B., Dror, I., Yaron, B., 2008. Contaminant partitioning in the aqueous phase. In: Contaminant Geochemistry, pp. 147–162.

Boccadoro, C., Krolicka, A., Receveur, J., Aepli, C., Floch, S.L., 2018. Microbial community response and migration of petroleum compounds during a sea-ice oil spill experiment in Svalbard. *Mar. Environ. Res.* 142, 214–233.

Bradford, J.H., Babcock, E.L., Marshall, H.-P., Dickins, D.F., 2015. Targeted reflection-waveform inversion of experimental ground-penetrating radar data for quantification of oil spills under sea ice. *Geophysics* 81 (1), WA59–WA70.

Brandvik, P.J., Faksness, L.-G., 2009. Weathering processes in Arctic oil spills: meso-scale experiments with different ice conditions. *Cold Reg. Sci. Technol.* 55 (1), 160–166.

Brandvik, P.J., Sørheim, K.R., Singass, I., Reed, M., 2006. Short state-of-the-art report on oil spills in ice-infested waters. Final. In: SINTEF A06148 Open Report No.: 1.

Brekke, C., Holt, B., Jones, C., Skrunes, S., 2014. Discrimination of oil spills from newly formed sea ice by synthetic aperture radar. *Remote Sens. Environ.* 145, 1–14.

Brown, C.E., Fingas, M.F., 2003. Review of the development of laser fluorosensors for oil spill application. *Mar. Pollut. Bull.* 47 (9), 477–484.

Canadian Council of Ministers of the Environment, 1999. Canadian water quality guidelines for the protection of aquatic life: polycyclic aromatic hydrocarbons (PAHs). In: Canadian Environmental Quality Guidelines, 1999. Canadian Council of Ministers of the Environment, Winnipeg.

Chen, L.-F., Ong, C.K., Neo, C.P., Varadan, V.V., Varadan, V.K., 2005. Microwave Electronics: Measurement and Materials Characterization.

Cox, G., Weeks, W., 1983. Equations for determining the gas and brine volumes in sea-ice samples. *J. Glaciol.* 29 (102), 306–316.

Desmond, D.S., 2018. Oil Behavior in Sea Ice: Changes in Chemical Composition and Resultant Effect on the Complex Permittivity (Dielectrics) and Radar Signature of Sea Ice. The University of Manitoba.

Desmond, D.S., Neusitzer, T.D., Isleifson, D., Saltymakova, D., Wolfe, T., Polciwiarke, K., Synder, N., Barber, D.G., Stern, G.A., 2018. Remote sensing of oil spills in a sea ice environment: investigations on oil composition and mitigation potential. In: Proceedings of the 2018 ArcticNet Annual Scientific Meeting, Ottawa, ON, CA.

Elam, S.K., Tokura, I., Saito, K., Altenkirch, R.A., 1989. Thermal conductivity of crude oils. *Exp. Thermal Fluid Sci.* 2, 1–6.

Engineering ToolBox, 2017. Hydrocarbons, linear alcohols and acids – density. [online]. Available at: https://www.engineeringtoolbox.com/density-alkane-alkene-benzene-carbon-number-alcohol-acid-alkyl-alkyne-d_1939.html.

Faksness, L.-G., Brandvik, P.J., 2008. Distribution of water soluble components from oil encapsulated in Arctic sea ice: summary of three field seasons. *Cold Reg. Sci. Technol.* 54 (2), 106–114.

Faksness, L.-G., Brandvik, P.J., Sydnes, L.K., 2008. Composition of the water accommodated fractions as a function of exposure times and temperatures. *Mar. Pollut. Bull.* 56 (10), 1746–1754.

Faksness, L.-G., Brandvik, P.J., Daee, R.L., Leirvik, F., Børseth, J.F., 2011. Large-scale oil-in-ice experiment in the Barents Sea monitoring of oil in water and MetOcean interactions. *Mar. Pollut. Bull.* 62 (5), 976–984.

Fingas, M., Brown, C.E., 2007. Oil spill remote sensing: a forensic approach. In: Oil Spill Environmental Forensics. Fingerprinting and Source Identification.

Fingas, M.F., Hollebone, B.P., 2003. Review of behaviour of oil in freezing environments. *Mar. Pollut. Bull.* 47 (9), 333–340.

Firoozy, N., 2015. Radar Cross Section Data Inversion for Snow-covered Sea Ice Remote Sensing. The University of Manitoba.

Firoozy, N., Mojabi, P., Barber, D.G., 2015. Nonlinear inversion of microwave scattering data for snow-covered sea-ice dielectric profile reconstruction. *IEEE Geosci. Remote Sens. Lett.* 12 (1), 209–213.

Firoozy, N., Neusitzer, T., Desmond, D.S., Tiede, T., Lemes, M., Landy, J., Mojabi, P., Rysgaard, S., Stern, G., Barber, D.G., 2017. An electromagnetic detection case study on crude oil injection in a young sea ice environment. *IEEE Trans. Geosci. Remote Sens.* 55 (8), 4465–4475.

Firoozy, N., Neusitzer, T., Chirkova, D., Desmond, D., Lemes, M., Landy, J., Mojabi, P., Rysgaard, S., Stern, G., Barber, D.G., 2018. A controlled experiment on oil release beneath thin sea ice and its electromagnetic detection. *IEEE Trans. Geosci. Remote Sens.* 56 (8), 4406–4419.

Fresco-Rivera, P., Fernández-Varela, R., Gómez-Carracedo, M.P., Ramírez-Villalobos, F., Prada, D., Muniategui, S., Andrade, J.M., 2007. Development of a fast analytical tool to identify oil spillages employing infrared spectral indexes and pattern recognition techniques. *Talanta* 74 (2), 163–175. <https://doi.org/10.1016/j.talanta.2007.05.047>.

Fritt-Rasmussen, J., Wegeberg, S., Gustavson, K., 2015. Review on burn residues from in situ burning of oil spills in relation to Arctic waters. *Water Air Soil Pollut.* 226 (10), 329.

Galley, R.J., Babb, D., Ogi, M., Else, B.G.T., Geilfus, N.-X., Crabeck, O., Barber, D.G., Rysgaard, S., 2016. Replacement of multiyear sea ice and changes in open water season duration in the Beaufort Sea since 2004. *J. Geophys. Res. Oceans* 121, 1806–1823.

Harslem, Ø., Eide, A., Heen, K., 2011. Factors influencing future oil and gas prospects in the Arctic. *Energy Policy* 39 (12), 8037–8045.

Isleifson, D., Galley, R.J., Barber, D.G., Landy, J.C., Komarov, A.S., Shafai, L., 2014. A study on the C-band polarimetric scattering and physical characteristics of frost flowers on experimental sea ice. *IEEE Trans. Geosci. Remote Sens.* 52 (3), 1787–1798. <https://doi.org/10.1109/tgrs.2013.2255060>.

Jones, M.D.H., Henderson-Sellers, A., 1990. History of the greenhouse effect. *Prog. Phys. Geogr.* 14 (1), 1–18.

Klamt, A., Jonas, V., Bürger, T., Lohrenz, J., 1998. Refinement and parametrization of COSMO-RS. *J. Phys. Chem. A* 102 (26), 5074–5085.

Kwok, R., Cunningham, G.F., Wensnahan, M., Rigor, I., Zwally, H.J., Yino, D., 2009. Thinning and volume loss of the Arctic Ocean sea ice cover: 2003–2008. *J. Geophys. Res.* 114, C07005. <https://doi.org/10.1029/2009JC005312>.

Lashof, D.A., 1989. The dynamic greenhouse: feedback processes that may influence future concentrations of atmospheric trace gases and climatic change. *Clim. Chang.* 14 (3), 213–242.

Leppäranta, M., Manninen, T., 1988. The Brine and Gas Content of Sea Ice With Attention to Low Salinities and High Temperatures.

Louwen, J.N., Pye, C., Lenthe, E.V., 2008. ADF2008. 01 COSMO-RS, SCM, Theoretical Chemistry. Vrije Universiteit, Amsterdam, The Netherlands (There is no corresponding record for this reference).

MacDonald, G.J., 1988. Scientific basis for the greenhouse effect. *Journal of Policy Analysis and Management* 7 (3), 425–444.

Maslanik, J.J., Stroeve, J., Fowler, C., Emery, W., 2011. Distribution and trends in Arctic sea ice age through spring. *Geophys. Res. Lett.* 38, L13502. <https://doi.org/10.1029/2011GL047735>.

Maus, S., Becker, J., Schneebeli, M., Wiegmann, A., 2015. Oil saturation of the sea ice pore space. In: Proceedings of the 23rd International Conference on Port and Ocean Engineering Under Arctic Conditions, (Web).

Montaron, B., 2012. Scale-independent mixing laws. arXiv.org [Mathematical Physics] 1–6 (1206.6560).

National Academies of Sciences, Engineering, and Medicine, 2016. Spills of Diluted Bitumen From Pipelines: A Comparative Study of Environmental Fate, Effects, and Response. The National Academies Press, Washington, DC.

Nemirovskaya, I.A., 2014. Hydrocarbons in the snow-ice cover of different areas of the White Sea. *Oceanology* 54 (3), 298–307.

Neusitzer, T.D., Firoozy, N., Tiede, T.M., Desmond, D.S., Lemes, M., Stern, G.A., Rysgaard, S., Mojabi, P., Barber, D.G., 2018. Examining the impact of a crude oil spill on the permittivity profile and normalized radar cross-section of young sea ice. *IEEE Trans. Geosci. Remote Sens.* 56 (2), 921–936. <https://doi.org/10.1109/tgrs.2017.2756843>.

Ni, N., Yalkowsky, S.H., 2003. Prediction of Setschenow constants. *Int. J. Pharm.* 254 (2), 167–172.

Nordam, T., Litzler, E., Ronningen, P., Aune, J., Hagelien, T.F., Luktu, A., Beegle-Krause, C.J., Bronner, U., 2018. Oil spill contingency and response modelling in ice-covered waters. In: Proceedings of the Forty-first AMOP Technical Seminar, Environment and Climate Change Canada, Ottawa, ON, Canada, pp. 957–973.

Oggier, M., 2014. Sea ice microstructure oil migration through brine channels. In: Alaska Oil Spill Technology Symposium, (Web).

Panuganti, S.R., Wang, F., Chapman, W.G., Vargas, F.M., 2016. A simple method for estimation of dielectric constants and polarizabilities of nonpolar and slightly polar hydrocarbons. *Int. J. Thermophys.* 37, 75.

Payne, J.R., Hachmeister, L.E., McNabb Jr., G.D., Sharpe, H.E., Smith, G.S., Manen, C.A., 1991a. Brine-induced advection of dissolved aromatic hydrocarbons to Arctic bottom waters. *Environ. Sci. Technol.* 25, 940–951.

Payne, J.R., McNabb Jr., G.D., Clayton Jr., J.R., 1991b. Oil-weathering behavior in Arctic environments. *Polar Res.* 10 (2), 631–662.

Petrich, C., Karlsson, J., Eicken, H., 2013. Porosity of growing sea ice and potential for oil entrainment. *Cold Reg. Sci. Technol.* 87, 27–32 (Web).

Petrich, C., O'Sadnick, M., Brekke, C., Myrnes, M., Maus, S., Salomon, M.L., Woelk, S., Grydeland, T., Janssen, R.O., Eicken, H., Oggier, M., Ferro-Famil, L., Harkati, L., Rebane, O., Reimer, N., 2018. An overview of the MOSIDEO/CIRFA experiments on behavior and detection of oil in ice. In: Proceedings of the Forty-first AMOP Technical Seminar, Environment and Climate Change Canada, Ottawa, ON, Canada, pp. 112–122.

Pringle, D.J., Eicken, H., Trodahl, H.J., Backstrom, L.G.E., 2007. Thermal conductivity of landfast Antarctic and Arctic sea ice. *J. Geophys. Res.* 112, 1–13.

Puestow, T., Parsons, L., Zakharov, I., Cater, N., Bobby, P., Fuglem, M., Parr, G., Jayasiri, A., Warren, S., Warbandski, G., 2013. Oil spill detection and mapping in low visibility and ice: surface remote sensing. In: Arctic Response Technology Oil Spill Preparedness, (Technical Report).

Pye, C.C., Ziegler, T., 1999. An implementation of the conductor-like screening model of solvation within the Amsterdam density functional package. *Theoretical Chemistry Accounts: Theory, Computation, and Modeling (Theoretica Chimica Acta)* 101 (6), 396–408.

Sadnick, M.O., Petrich, C., Phuong, N.D., 2017. The entrainment and migration of crude oil in sea ice, the use of vegetable oil as a substitute, and other lessons from laboratory experiments. In: Proceedings of the 24th International Conference on Port and Ocean Engineering Under Arctic Conditions.

Saltymakova, D., Desmond, D.S., Firoozy, N., Neusitzer, T.D., Xu, Z., Barber, D.G., Stern, G.A., 2019. Chemical Partitioning of Crude Oil in First-year Ice and Its Impact on Sea Ice Geophysics. (in prep). (To be submitted to Marine Pollution Bulletin).

Scheibye, K., Christensen, J.H., Johnsen, A.R., 2017. Biodegradation of crude oil in Arctic subsurface water from the Disko Bay (Greenland) is limited. *Environ. Pollut.* 223, 73–80.

Schenk, C.J., 2011. Geology and petroleum potential of the West Greenland–East Canada Province. *Geological Society, London, Memoirs* 35.1, 627–645.

Schwarz, L., Frimmel, A., 2004. Chemostratigraphy of the Posidonia Black Shale, SW-Germany: II. Assessment of extent and persistence of photic-zone anoxia using aryl isoprenoid distributions. *Chem. Geol.* 206 (3), 231–248.

Sharing Earth Observation Resources RADARSAT-2. [online]. Available at: <https://directory.eoportal.org/web/eoportal/satellite-missions/r/radarsat-2>.

Simecek-Beatty, D., Lehr, W.J., 2007. Trajectory modeling of marine oil spills. *Oil Spill Environmental Forensics* 405–418.

Smith, L.C., Stephenson, S.R., 2013. New Trans-Arctic shipping routes navigable by midcentury. *Proc. Natl. Acad. Sci.* 110 (13), E1191–E1195.

Stogryn, A., Desargant, G.D., 1985. The dielectric properties of brine in sea ice at microwave frequencies. *IEEE Trans. Antennas Propag.* AP-33 (5), 523–532 (May 1985).

Stout, S.A., Wang, Z., 2016. Photochemical effects on oil spill fingerprinting. In: *Standard Handbook Oil Spill Environmental Forensics: Fingerprinting and Source Identification*, 2nd. Elsevier, Academic Press.

Swaby, L.G., Forzati, A.F., 1969. Remote sensing of oil slicks. In: *International Oil Spill Conference*. vol. 1969 American Petroleum Institute No. 1.

Ulaby, F.T., Long, D.G., Blackwell, W., Elachi, C., Fung, A., Ruf, C., Sarabandi, K., Zyl, J.V., Zebker, H., 2014. *Microwave Radar and Radiometric Remote Sensing*. vol. 6.

Van Dyck, C., Marks, T.J., Ratner, M.A., 2017. Chain length dependence of the dielectric constant and polarizability in conjugated organic thin films. *ACS Nano* 11, 5970–5981.

Vergeynst, L., Christensen, J.H., Kjeldsen, K.U., Meire, L., Boone, W., Malmquist, M.V., Rysgaard, S., 2019. In situ biodegradation, photooxidation and dissolution of petroleum compounds in Arctic seawater and sea ice. *Water Res.* 148, 459–468.

Walsh, J.E., Anisimov, O., Hagen, J., Jakobsson, T., Oerlemans, J., Prowse, T.D., Romanovsky, V., Savelieva, N., Serreze, M., Shiklomanov, A., Shiklomanov, I., Solomon, S., 2005. Chapter 6: cryosphere and hydrology. In: *Arctic Climate Impact Assessment*, (np).

Wang, Z., Stout, S.A., 2007. Chemical fingerprinting of spilled or discharged petroleum—methods and factors affecting petroleum fingerprints in the environment. In: *Oil Spill Environmental Forensics: Fingerprinting and Source Identification*, pp. 1–53.

Wiese, F.K., Robertson, G.J., Gaston, A.J., 2004. Impacts of chronic marine oil pollution and the murre hunt in Newfoundland on thick-billed murres *Uria lomvia* populations in the eastern Canadian Arctic. *Biol. Conserv.* 116 (2), 205–216.

Wilkinson, J.P., Boyd, T., Hagen, B., MakSYM, T., Pegau, S., Roman, C., Singh, H., Zabilansky, L., 2015. Detection and quantification of oil under sea ice: the view from below. *Cold Reg. Sci. Technol.* 109, 9–17.

Word, J.Q., Word, L.S., Gardiner, W.W., Word, J.D., McFarlin, K.M., Perkins, R.A., 2011. “Joint Industry Program to Evaluate Biodegradation and Toxicity of Dispersed Oil in Cold Water Environments of the Beaufort and Chukchi Seas.” Phase 1 and 2 Final Report.

Xiong, R., Sandler, S.I., Burnett, R.I., 2014. An improvement to COSMO-SAC for predicting thermodynamic properties. *Ind. Eng. Chem. Res.* 53 (19), 8265–8278.

Yu, X., Yu, R., 2013. Setschenow constant prediction based on the IEF-PCM calculations. *Ind. Eng. Chem. Res.* 52 (32), 11182–11188.